

More concentrated precipitation decreases terrestrial water storage

<https://doi.org/10.1038/s41586-026-10487-7>

Corey S. Lesk^{1,2,3✉} & Justin S. Mankin^{1,4,5}

Received: 31 May 2025

Accepted: 2 April 2026

Published online: 13 May 2026

Open access

 Check for updates

Terrestrial water availability is a key determinant of human and ecosystem well-being^{1,2}. Apart from mean precipitation and evaporation changes^{3,4}, it is unknown how daily-scale precipitation concentration into fewer, heavier events affects hydrologic partitioning and the land water balance^{5–9}. Here we show observationally that more concentrated precipitation decreases land water availability across all climates globally, a drying effect as strong in magnitude as the wetting effect of increased total precipitation. Simple and complex land-surface models recover the observed effect, whereas idealized simulations show that it arises from enhanced evaporation caused by hydrologic partitioning changes at the land surface. Projected terrestrial water storage impacts of warming-driven precipitation concentration at about 2 °C of warming shift the land surface to abnormally dry conditions (≥ 0.5 standard deviation¹⁰) for 27% of the global population, independent of any total precipitation or irrigation changes. Our results show new key determinants of the land water balance, highlighting its sensitivity to the temporal distribution of precipitation, with broad implications for future water availability.

The land water balance is essential for the well-being of ecosystems and people^{1,2}. Yet, its future is uncertain because of sparse observations and a lack of theory unifying climate and hydrologic changes^{11,12}. Although water availability emerges from the balance of mean precipitation and evaporation, a key uncertainty resides with how warming-forced changes to the character and distribution of daily precipitation will alter the long-term land water balance. The right-skewed daily precipitation distribution means a minority of days contribute most to annual precipitation¹³. At the same time, the highest percentiles of this distribution are over three times more sensitive to warming than annual mean precipitation itself ($>7\% \text{ K}^{-1}$ compared with about $2\% \text{ K}^{-1}$)^{5,14}. The asymmetry in the precipitation distribution and its unequal response to warming implies a concentration of rain and snow into fewer, more intense and localized events, separated by longer dry intervals, with ambiguous implications for terrestrial water availability^{5–9,15,16}.

Debates over future aridity tend to focus on the climatological precipitation–evaporation balance^{3,4}, whereas research on the impacts of precipitation intensification generally centre on flood risks^{17,18}. Yet precipitation concentration could exert an important control on the climatological land water balance by reshaping hydrologic partitioning of rain and snow into rivers, soils and vegetation. Saturation and infiltration excess runoff on the land, for example, can be controlled by the duration and intensity of rainfall, whereas the dry intervals between rain events articulate the energetic space for evapotranspiration. Experimental treatments in a US grassland, for example, found reduced soil moisture in response to more concentrated watering¹⁹, whereas daily rainfall variability affected satellite vegetation indices over 42% of vegetated lands²⁰. But the extent, spatial pattern and magnitude of the impact of precipitation concentration

on climatological water availability, both historically and in future climates, remain unknown.

We analyse the observational relationship between satellite-derived annual-scale terrestrial water storage (TWS) anomalies and precipitation concentration estimated by a Gini coefficient with multiple precipitation datasets^{21–23}. The annual Gini coefficient of daily precipitation quantifies how evenly precipitation falls over a year. Our empirical models demonstrate that precipitation concentration reduces continental water availability across all climates globally. The magnitude of the drying effect of concentration on TWS variability rivals the effect of total annual precipitation itself, suggesting a first-order control of precipitation concentration on the land water balance, beyond the long-term balance between precipitation and evapotranspiration.

Using a simple land-surface model that captures the nonlinear behaviour among energy and moisture, we then reproduce our empirical results and show that precipitation concentration enhances evaporation through changes in surface hydrologic partitioning and increased shortwave radiation between precipitation events—consistent with first-principles of land–atmosphere interactions. These observed and idealized results are also consistent with the response in more complex land-surface components of Earth system models. Finally, we combine our empirical model with observed and projected concentration trends to estimate historical and future TWS impacts. Wherever possible, we rely on observations given known deficiencies in daily precipitation simulation by global atmospheric models. Our findings indicate that the utility of precipitation for land water availability depends as much on its high-frequency distribution as on its annual total and that this utility decreases under warming.

¹Department of Geography, Dartmouth College, Hanover, NH, USA. ²Neukom Institute for Computational Science, Dartmouth College, Hanover, NH, USA. ³Department of Earth and Atmospheric Science, Université du Québec à Montréal, Montreal, Quebec, Canada. ⁴Department of Earth & Planetary Sciences, Dartmouth College, Hanover, NH, USA. ⁵Division of Ocean and Climate Physics, Lamont-Doherty Earth Observatory, Columbia University, New York, NY, USA. ✉e-mail: lesk.corey@uqam.ca

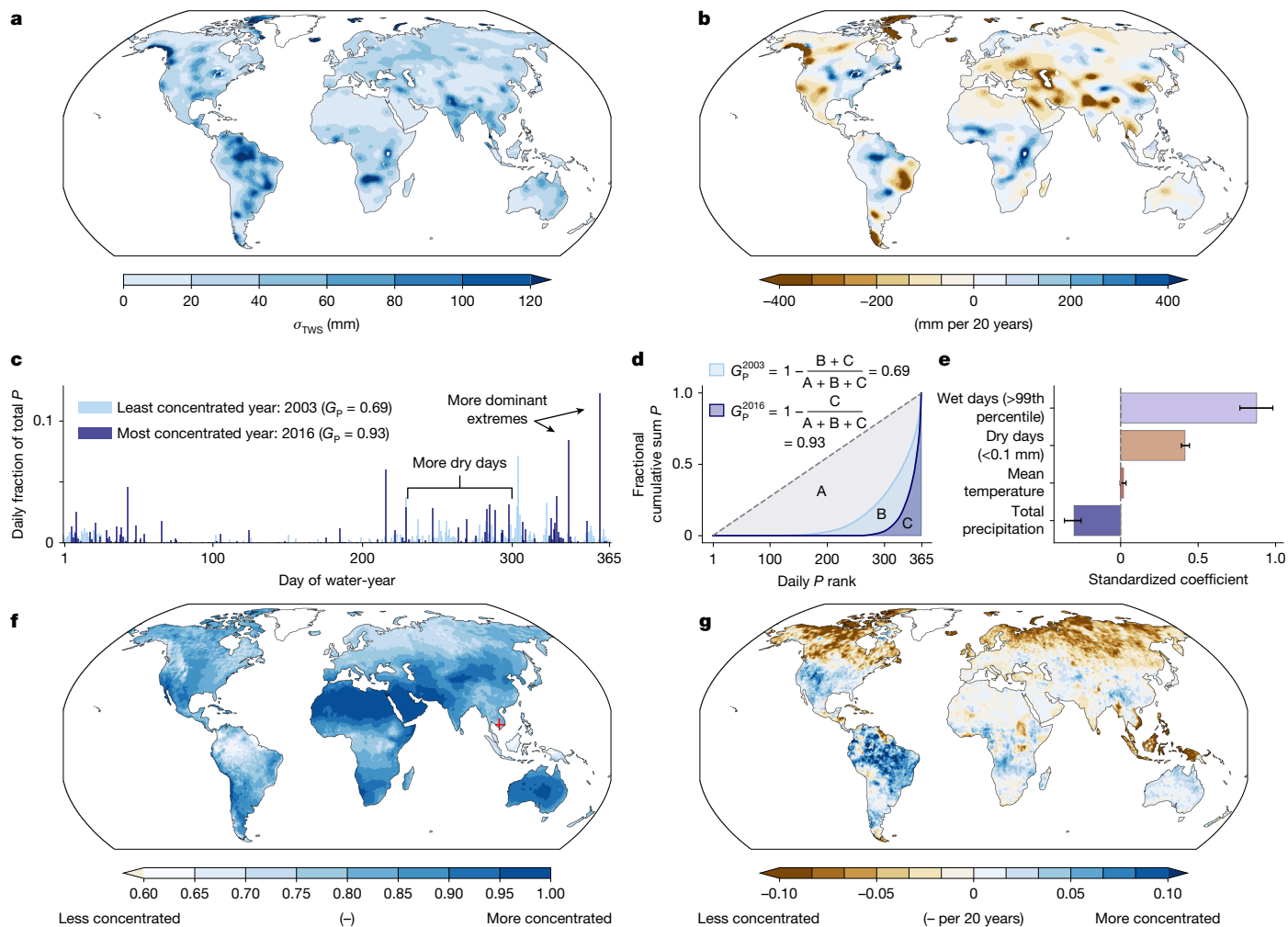


Fig. 1 | Trends and variability in TWS and rainfall concentration. **a**, Standard deviation of detrended water-year mean TWS from GRACE satellite observations²⁵, over 2002–2022. **b**, Linear trend in water-year mean GRACE TWS over 2002–2022, shown as change per 20 years. **c**, Illustrative daily precipitation time series from Phnom Penh, Cambodia, for water-years 2003 (light blue) and 2016 (dark blue), the years with maximum and minimum daily precipitation concentrations, respectively, in the study period as quantified using the Gini coefficient. Data are from the Climate Prediction Center (CPC)²². Annotations indicate contrasting features of concentration in 2016 compared with 2003. **d**, Lorenz curves (fractional cumulative sum of ranked daily precipitation) for the two time series in **a** (light and dark blue). The grey dotted line shows the hypothetical Lorenz curve for equal daily precipitation. The daily precipitation Gini coefficient (G_p) is calculated from the shaded

integrals A, B and C, as annotated. **e**, Global dependence over 2002–2022 among interannual variations in G_p and key hydroclimate variables, including extreme precipitation days (exceeding the 99th percentile of climatological nonzero daily precipitation), dry days (days with less than 0.1 mm precipitation), annual mean 2 m air temperature and annual total precipitation. Error bars show the range of estimates across three precipitation data products. **f**, Mean G_p over 1980–2022, with the location of Phnom Penh indicated with a red cross. **g**, G_p trends over 1980–2022, expressed as changes per 20 years. Data shown in **f** and **g** averages across the CPC, Global Precipitation Climatology Center (GPCC)²³ and Global Precipitation Climatology Project (GPCP)²¹ daily precipitation datasets; results for individual data products are shown in Extended Data Fig. 3. Base map adapted from Natural Earth (<https://www.naturalearthdata.com>).

Terrestrial water and precipitation concentration

Since 2002, the Gravity Recovery and Climate Experiment (GRACE) satellite has provided a record of TWS anomalies, capturing observed variations of water held in soils, aquifers, vegetation and surface bodies^{24,25} (Fig. 1a). The emergent climatological record from GRACE has positioned analyses on drivers of the land water balance^{26,27} and its couplings to wider ecosystem processes²⁸ and climate feedbacks²⁹. The interannual standard deviation in TWS (σ_{TWS}) ranges between approximately 10 mm and 100 mm across global land areas (Fig. 1a), whereas its 2002–2022 long-term trends are of mixed sign spatially (Fig. 1b). The ice-loss-driven declines in Patagonia, Alaska, the Himalaya and the Arctic Cordillera (around 500 mm over 2002–2022); wetting in the Sahel and Amazon (about 300 mm)³⁰; and groundwater depletion in northern India and the North China Plain³¹ are evident. For our subsequent analyses, we remove these long-term trends to isolate

interannual variability. We also omit Greenland and Antarctica because of the dominant influence of their ice caps.

To assess daily-scale precipitation concentration and its change over time, we adapt the Gini coefficient (originally used in economics to assess income inequality) to summarize the inequality in the daily distribution of annual precipitation across three precipitation datasets (Fig. 1c,d). The daily-scale precipitation Gini coefficient (G_p) ranges from 0 (equal daily precipitation) to 1 (all precipitation falling in a single day). We illustrate its calculation and interpretation for Phnom Penh, Cambodia, because of the stark difference between its least (2003, $G_p = 0.69$) and most (2016, $G_p = 0.93$) concentrated year in our study period (Fig. 1c,d). The high concentration in 2016 is evident from longer dry periods, higher mean event intensity and the dominance of extreme events (>5% of annual precipitation, Fig. 1c). The fractional sorted cumulative sum of these time series forms their Lorenz curves (Fig. 1d, light and dark blue), with annual G_p defined as

the area between the Lorenz curve and the one-to-one line of perfect equality (Fig. 1d, grey dotted line).

Globally, interannual G_p variation is strongly and statistically significantly associated with both wet days (>99th percentile) and dry days (<0.1 mm, $P < 0.001$; Fig. 1e). Precipitation concentration is ubiquitously negatively related to total precipitation ($P < 0.001$; Fig. 1e and Extended Data Fig. 1), but shows little dependence on mean temperature. The three observational precipitation datasets agree on these drivers (Fig. 1e). Although precipitation on Earth is generally quite concentrated¹³, its spatial variation falls along climate classes, with less concentration in humid regions (high latitudes, deep tropics, $G_p \approx 0.7$) and more concentration in deserts ($G_p \approx 1$; Fig. 1f and Extended Data Figs. 2 and 3). Since the 1980s, G_p trends are of mixed sign, decreasing to be less concentrated in high latitudes and in Southeast Asia, but increasing in the western USA, northern South America and Central Africa^{5,8,16} (Fig. 1g and Extended Data Fig. 3). Reduced concentration in the northern high latitudes is consistent with strong mean annual precipitation increases much closer to the intensity scaling rates³², which enable intensification without increased intermittency.

Drying effect of precipitation concentration

We expect that higher G_p values are associated with lower TWS, as hydrologic partitioning preferences evapotranspiration to the detriment of soil and land water recharge. More intense precipitation is more likely to exceed soil infiltration capacity, increasing ponded surface water, a more easily evaporable pool. Furthermore, evaporation from such surface water stocks is enhanced by longer dry spells, attendant high incident shortwave radiation and lower surface resistance to evaporation compared with over soils and vegetation.

To test these hypotheses, we use a panel regression model with fixed effects commonly used in causal inference. We link observed interannual variation in TWS to that for G_p , with controls for annual total precipitation and mean temperature to isolate the influence of rainfall concentration absent other drivers of TWS variability (Fig. 1e). Our fixed-effects regression model interacts G_p with average total precipitation to explicitly assess variation in the effect of G_p on TWS across the global aridity gradient. It also controls both for unobserved spatially varying factors that might be consistent across time (such as land surface properties or groundwater usage) and any time-varying shocks or trends that are common across all places (such as modes of variability such as El Niño–Southern Oscillation or anthropogenic warming). As such, the identification strategy we use characterizes the relationship between G_p and TWS anomalies conditioned on mean precipitation, providing an estimate of the causal relationship between the two (Methods).

Higher G_p is statistically significantly associated with negative TWS anomalies across all climatological precipitation values globally, indicating a drying effect of precipitation concentration on water availability (Fig. 2 and Supplementary Table 2). Standardizing the effects across terms shows that the G_p effect is comparable—but of opposite sign—to the effect of total annual precipitation itself ($-0.16\sigma_{\text{TWS}}/\sigma_{G_p}$, compared with $0.2\sigma_{\text{TWS}}/\sigma_P$ at the global population-weighted climatological mean precipitation of 1,000 mm) (Fig. 2a). Furthermore, the drying effect of G_p is about three times larger than that of temperature. These results are consistent across the three precipitation datasets, indicating a robust, leading-order influence of the distributional character of precipitation—irrespective of its annual total—on TWS.

The magnitude of the G_p effect on TWS varies with climatological mean precipitation, with larger magnitudes of TWS loss from precipitation concentration in wetter climates (Fig. 1b). However, the drying effect of precipitation concentration is universally and significantly negative, ranging from about 10 mm to 30 mm per 10 percentage-point change in G_p ($0.1\Delta G_p$) in deserts to about 20–130 mm per $0.1\Delta G_p$ in very humid climates. At 1,000 mm of annual mean precipitation, the

effect is 16–49 mm per $0.1\Delta G_p$ (Fig. 2b, vertical dotted line). Comparing these absolute estimates to the interannual standard deviation of TWS (of the order of 10–100 mm; Fig. 1a), the drying effect of G_p is substantial, ranging from 0.4 to nearly 3 standard deviations (σ_{TWS}) per $0.1\Delta G_p$ (Extended Data Fig. 4). When normalized by TWS variability, the relative G_p effects on TWS are larger in arid (mean annual precipitation <500 mm) and very humid (>2,000 mm) climates, and smaller in humid climates (500–2,000 mm per year; Extended Data Fig. 4).

We find consistent drying effects of G_p on TWS even when the empirical model is instead estimated at the river basin scale on which hydrologic mass closure occurs (Fig. 2c and Extended Data Fig. 5). Across the three precipitation datasets, G_p effects on TWS are statistically significant across 84% of global river basins, 80% of which are negative. Some of the most economically and ecologically important global river basins exhibit a drying effect of rainfall concentration, including the Amazon, Nile, Mississippi, Ganges and Yangtze. However, we note a few exceptions in which more concentrated rainfall increases TWS, notably in the Lake Chad and Volta basins.

Irrigation has influenced TWS locally, particularly as groundwater extraction has intensified in recent decades. We find a localized influence of interannual variation in irrigation on the G_p effect on TWS. The drying effect of G_p is amplified in the most intensively irrigated regions ($\geq 10\%$ of area equipped for irrigation; Extended Data Fig. 6a, darker blue lines), but TWS effects are indistinguishable from the global average over the 95% of land area that is not intensively irrigated (<10% of area equipped for irrigation; Extended Data Fig. 6a, lighter blue lines). We find no significant relationship between TWS effects and area equipped for irrigation at the river basin scale (Extended Data Fig. 6b). These results suggest that more concentrated precipitation dries the land globally as an intrinsic feature of hydroclimate, irrespective of irrigation. However, farmer responses to drying may locally amplify this drying by groundwater extraction.

Mechanisms of land drying

To explain the drying effect of precipitation concentration on TWS, we analyse how key water and energy budget terms depend on G_p within our empirical framework (Fig. 3). Concentration necessarily implies increased dry days between precipitation events (Fig. 1e); it also implies higher net surface shortwave radiation overall, a response we confirm in the annual mean using the GEWEX-SRB and NASA-EBAF radiation budgets (the average effect across these two datasets is shown in Fig. 3a). The average water-year marginal effect of G_p on shortwave radiation ranges from 1 W m^{-2} to 10 W m^{-2} per $0.1\Delta G_p$ and is statistically significant in climates with annual precipitation up to about 2,000 mm, beyond which its effects are ambiguous, probably because of ubiquitous daily precipitation in those humid climates.

The number of dry and heavy precipitation days both increase during higher- G_p years, suggesting at least two mechanisms by which concentration affects the land water balance. The first mechanism is radiative: additional dry days allow more shortwave radiation (a key driver of evaporation) to reach the surface, regardless of changes in precipitation intensity. The second mechanism relates to the impact of the temporal distribution of the precipitation on hydrologic partitioning, with intensified precipitation favouring the partitioning of water to more evaporable reservoirs. To isolate this latter intensity-partitioning effect, we regress TWS on G_p while controlling for shortwave radiation anomalies, effectively removing the covarying impact of additional dry days. We then compare this effect to the full TWS effect from Fig. 2b, which includes both the radiative and intensity-partitioning effects (Fig. 3b and Supplementary Fig. 1).

The intensity-partitioning effect of G_p on TWS through changes in hydrologic partitioning is statistically significant and negative in all but the most humid climates in which climatological precipitation exceeds 3,000 mm (Fig. 3b, blue line and shaded interval). This

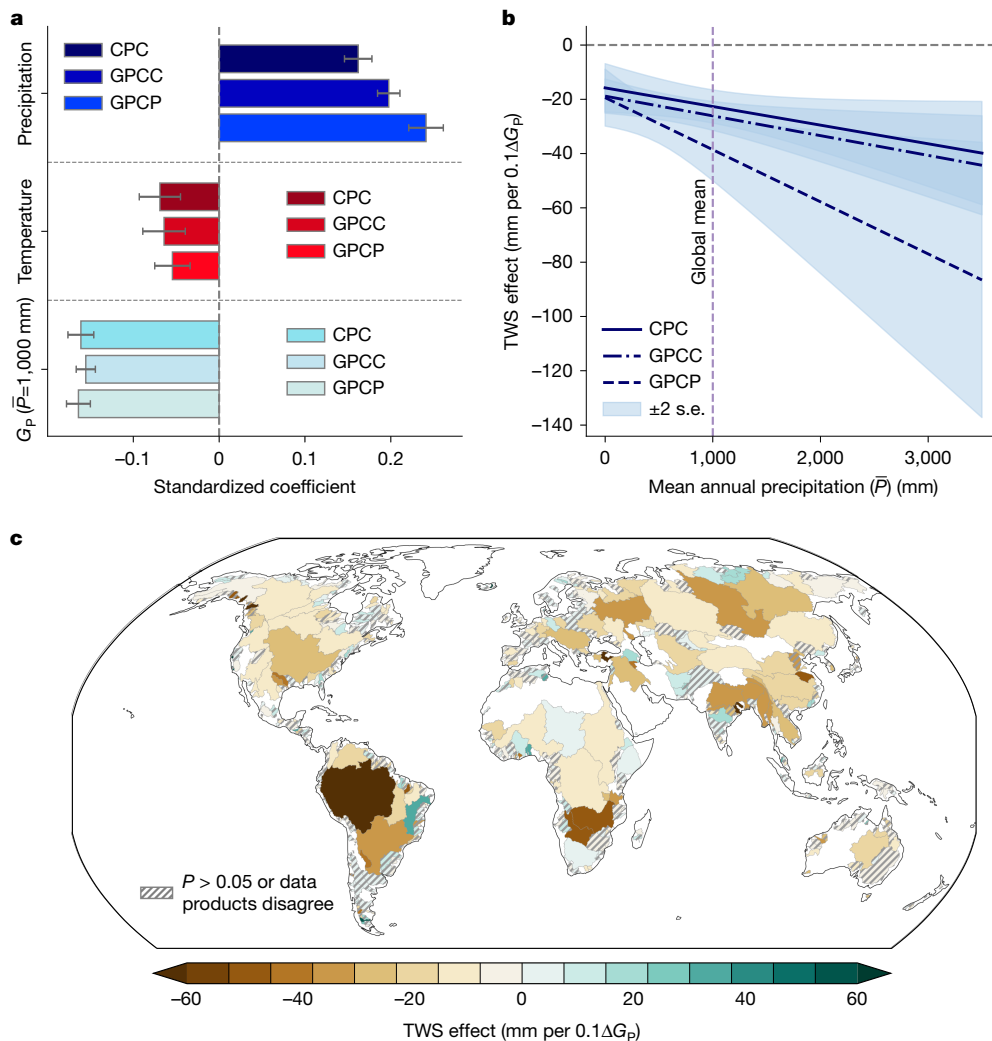


Fig. 2 | Land-drying effect of more concentrated precipitation.

a, Standardized regression coefficients of water-year total precipitation (dark blue), mean 2 m air temperature (red) and daily rainfall Gini coefficient (G_p , light blue) anomalies on GRACE TWS²⁵ anomalies. The effect of G_p on TWS, being conditional on climatological mean precipitation, is shown for mean precipitation of 1,000 mm (the global population-weighted mean). Error bars show 2 standard errors of the estimate. **b**, Marginal effect of G_p on TWS,

conditional on mean precipitation, for three precipitation data products. Shaded areas show 2 standard errors of the estimate. **c**, Marginal G_p effects on TWS estimated at the scale of HydroSHEDS main river basins³¹, averaged across the three data products. Results for individual data products are shown in Extended Data Fig. 5. Effects are significant at $P < 0.05$ and of like sign across in at least two of the three data products, except in hatched basins. Base map adapted from Natural Earth (<https://www.naturalearthdata.com>).

intensity-partitioning effect accounts for nearly all of the full G_p -TWS effect (Fig. 3b, black lines) in arid climates, but weakens with increasing climatological precipitation (Fig. 3b,c). This result highlights that the radiative effect is minimal where evaporation is limited by water and sizeable where evaporation is limited by energy, consistent with theory^{33,34}. Nevertheless, changes in hydrologic partitioning from precipitation intensity are more important than the additional short-wave radiation across all climates, accounting for more than 50% of the full effect (Fig. 3c). The weaker relative contribution of radiative anomalies is, in part, a function their small magnitude (of the order of 1% of annual mean insolation; Fig. 3a). These results are consistent across the GEWEX-SRB and the NASA-EBAF radiation budgets individually, although the tendency for greater dominance of the intensity-partitioning effect in more arid climates is clearer in the former (Supplementary Fig. 1).

Thus, the drying effect of more concentrated precipitation is mainly attributable to its arrival at the surface in more intense but more intermittent bursts, with likely attendant changes in surface precipitation partitioning, regardless of the fact that greater intermittency implies sunnier conditions on average. In short, the time distribution of daily

rainfall itself is chiefly responsible for the drying effect of G_p , whereas the consequent radiative effects are secondary, but gain importance in wetter (more energy-limited) climates.

As reliable evaporation observations are not globally available, we analyse simulated evaporation from the Global Land Evaporation Amsterdam Model (GLEAM) to assess whether evaporation explains the drying effect of G_p on TWS. We find some support for our proposed positive relationship of G_p and evaporation: two of three datasets are consistent with expectations, showing significant evaporation increases (about 10–200 mm per 0.1 ΔG_p) in subhumid to humid climates. In very arid regions, in which evaporation is always water-limited, evaporation shows small annual-scale decreases (Fig. 3d), suggesting even more water-limited conditions. However, as GLEAM incorporates reanalysis-based precipitation data with known biases, we interpret these results cautiously. Still, these results indicate that heightened evaporation may plausibly drive G_p -induced TWS drying, especially outside arid zones.

Because of the observational limits to identifying culpable mechanisms, we also test whether enhanced evaporation causes G_p -induced TWS drying using an idealized land-surface model forced with observed

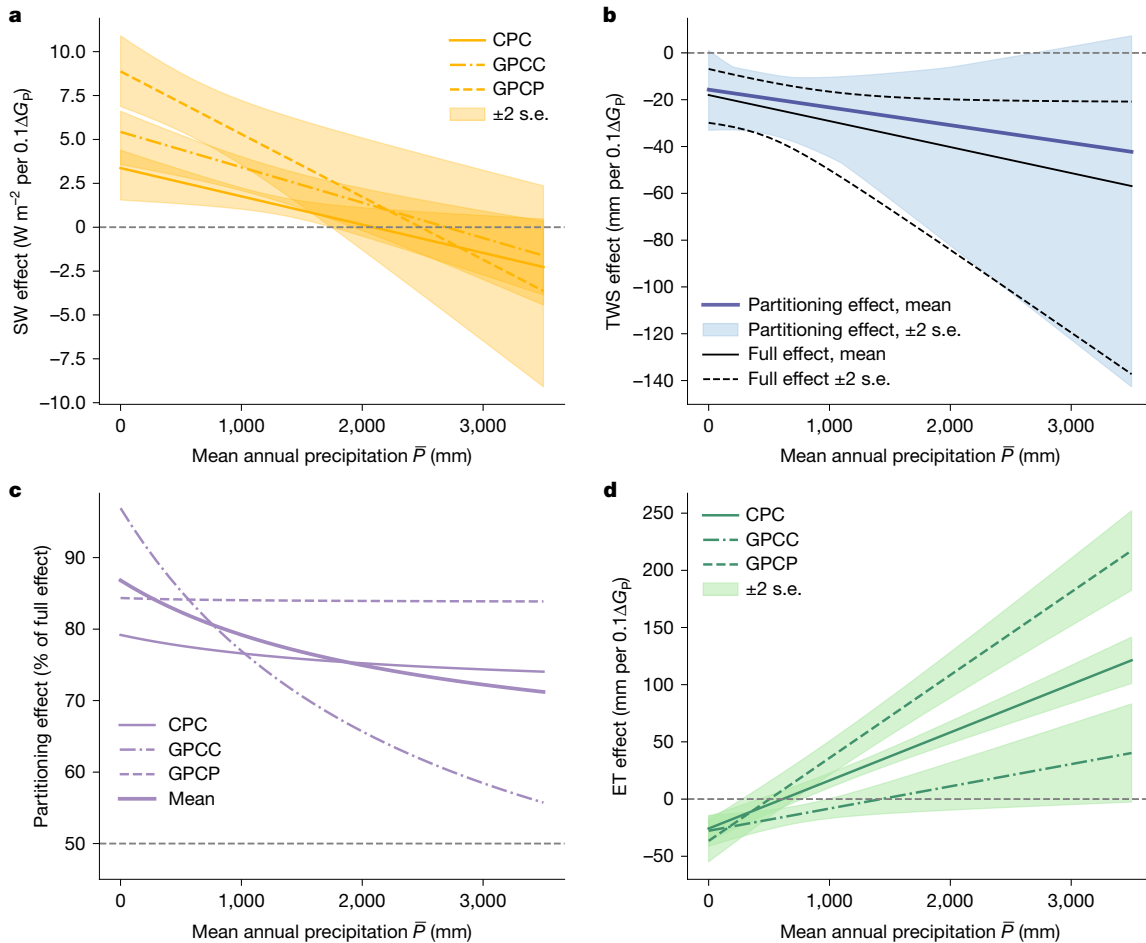


Fig. 3 | Mechanism of concentration effects on TWS. **a**, Dependence of water-year mean net surface shortwave (SW) radiation on the daily rainfall Gini coefficient (G_p), conditional on climatological mean precipitation. **b**, Marginal G_p effect on TWS controlling for shortwave radiation anomalies, to isolate the effect of temporal precipitation distribution, averaged across the three precipitation data products (blue line). The full G_p effect on TWS from Fig. 2 is shown in black, for comparison, with dotted lines showing full range covered by 2 standard errors of the estimate across data products. **c**, Intensity-partitioning

effect contribution to the full effect of G_p on TWS, estimated as the ratio of median distribution to full effects, for the mean of the three precipitation data products (thick solid line) and individually. In **a–c**, the average effect across the GEWEX-SRB⁵² and NASA-EBAS⁵³ radiation budget datasets is shown; results for individual data products are shown in Supplementary Fig. 1. **d**, Marginal effect of G_p on water-year total simulated evaporation (ET) from GLEAM⁵⁴, conditional on climatological mean precipitation. The shaded areas in **a**, **b** and **d** show 2 standard errors of the estimate.

daily precipitation and shortwave radiation data (Extended Data Figs. 7 and 8). The model, which simulates the land water balance given non-linear interactions between energy and water at the land–atmosphere interface, is run at about 1,500 grid points to sample across the observed global climatological precipitation gradient. The simulations position a direct comparison to our observationally derived effect of G_p on TWS (Fig. 4a–c). Our experimental approach is to identify the minimal physics required to reproduce the observed effect and to facilitate a scrutable diagnosis of culpable mechanisms. These goals are difficult to achieve in more complex land-surface models, in which the many processes and parameters forced with transiently evolving climate make it difficult to assess the drivers of a given response. However, we also analyse land-surface reanalyses from more complex land-surface models, finding consistent responses (Fig. 4d).

Our simulated TWS response to precipitation concentration (Fig. 4a; blue lines) recovers the observed effect from Fig. 2b (Fig. 4a, black lines), with both sets of confidence intervals overlapping for all climatological precipitation values. Tracking water budget terms in our idealized land model (Fig. 4b,c) supports the evaporation-driven mechanism suggested by our empirical analysis (Fig. 3). In higher- G_p years, more precipitation ponds at the surface (light blue curve, Q_s), and this surface excess water readily evaporates (green curve, E_s) rather than running

off the land (Fig. 4b, dark blue curve, Q_L , and Extended Data Fig. 7). At the same time, reduced infiltration suppresses soil evaporation (E_s , brown curve), but not enough to offset increased evaporation from the simulated surface water stock (M_L , Fig. 4b). As a result, total evaporation ($\Delta E = \Delta E_s + \Delta E_L$) increases in higher- G_p years (about 240 mm per 0.1Δ G_p ; Fig. 4b,c), in general agreement with empirical results from GLEAM (Fig. 3d).

We explore the sensitivity of these results by jointly perturbing all of the free parameters in the idealized model, producing about 365,000 simulations. The perturbed-parameter ensemble shows that the consilience between our empirical and process-based models is insensitive to parameter choices (Fig. 4a, orange shaded areas). A variance-based decomposition of parametric uncertainty emphasizes the importance of the geometry parameters controlling the depth and area of the surface water stock—these two parameters account for approximately 99% of the modelled variance in TWS drying (Supplementary Fig. 3). The magnitude of TWS drying is, therefore, most sensitive to the spatial extent of ponded surfaces after heavy rain events, reflecting the dominant role of G_p in shaping hydrologic partitioning at the surface and driving evaporation from surface water stocks. However, the overall drying effect of G_p remains robust across all tested surface geometries.

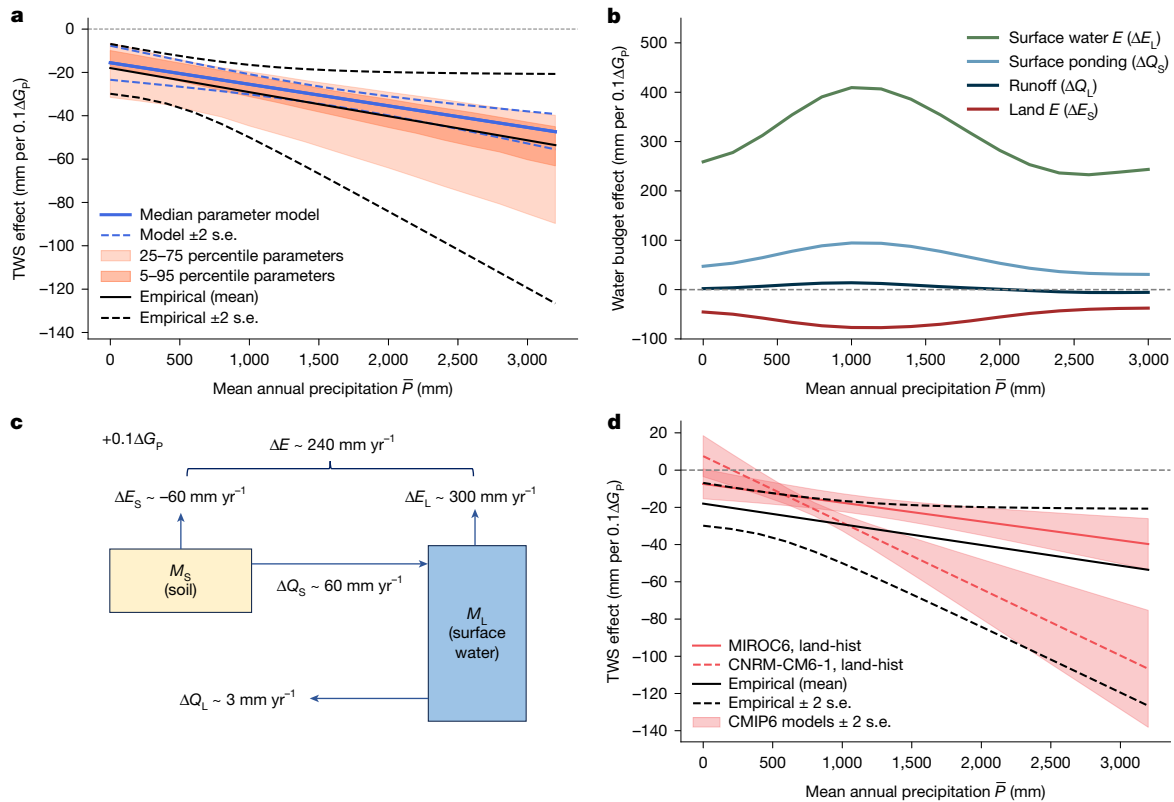


Fig. 4 | Drying effect of precipitation concentration in land-surface simulations. **a**, Effect of daily precipitation Gini coefficient (G_p) on TWS, as simulated by an idealized land-surface model at a sample of around 1,500 grid points across the mean annual precipitation distribution (solid blue line). The dotted blue lines show 2 standard errors of the estimated fit between the TWS effect and climatological mean precipitation. The shaded dark and light orange areas show the 5th–95th and 25th–75th percentile ranges of the same simulated effects across a 243-member perturbed-parameter ensemble. The black lines show the full empirical TWS effect from Fig. 2b, averaged across the three precipitation data products, for comparison. **b**, G_p effect on key water budget

terms, including evaporation from surface water reservoirs (green), surface ponding rate (precipitation less infiltration, light blue), runoff (dark blue) and land evaporation (brown). **c**, Schematic visualizing the same G_p effects on water budget terms as in **b**, on average across the mean annual precipitation domain. **d**, G_p effect on TWS, as simulated by the MIROC6 and CNRM-CM6-1 climate models under the land-hist experiment (land component of the models forced by observations, 1960–2014) from the Coupled Model Intercomparison Project, phase 6, Land Surface, Snow and Soil Moisture Model Intercomparison Project (CMIP6-LS3MIP)⁵⁵.

We also find a consistent G_p effect on TWS in the more complex land-surface components of the MIROC6 and CNRM-CM6-1 climate models, forced by historical observations (Fig. 4d). This suggests that climate models may accurately capture the TWS effect in future hydroclimate projections, provided they reliably simulate daily precipitation variability in fully coupled mode. Most fundamentally, the consistency among our observational, idealized and full-complexity model results indicates that more concentrated precipitation dries the land by partitioning water into easily evaporated pools through saturation- and infiltration-excess processes. Our simple land model reproduces empirical drying effect of the precipitation concentration on the land, indicating that its mechanism is traceable to elementary land-atmosphere dynamics.

Past and future implications

Observed G_p trends have affected TWS over recent decades (Fig. 5 and Extended Data Fig. 3). We estimate this impact by convolving the historical G_p trend field (around 1980–2022; Fig. 1g) with our empirical G_p –TWS relationship (Fig. 2b). The results reflect the spatial pattern of G_p trends (Fig. 5a), with slightly more (about 5%) of the global population experiencing G_p -driven drying than G_p -driven wetting (Fig. 5a, inset). As these results are based on detrended anomalies of the same data, the G_p -driven effects are already embedded in long-term TWS trends. As such, our results indicate that increasing precipitation concentration

has, for example, partly offset wetting trends in Amazonia and worsened drying trends in southeastern Brazil (Figs. 1b and 5a).

Although historical G_p -driven TWS impacts are mixed, continued warming should further concentrate precipitation into fewer, heavier events⁵⁸. Using a simple thermodynamic model of precipitation intensification (Methods), we estimate G_p changes under 1 °C of additional warming (about 2 °C above pre-industrial temperatures; Extended Data Fig. 9). We then combine these changes with our empirical model to project future mean TWS changes under future precipitation concentration. Our approach assumes that current irrigation practices hold into the future; yet the association between historical irrigation and TWS suggests that future irrigation intensification and expansion would exacerbate projected TWS drying, whereas increased irrigation efficiency could alleviate it (Methods and Extended Data Fig. 6a,b). Although the future balance of these effects over irrigated lands is unknown, they will all occur against a backdrop of physically based G_p -driven TWS drying.

We project widespread relative TWS reductions from future rainfall concentration alone, with 50% of the global population experiencing drying of $\geq 1/3\sigma_{TWS}$ and 27% of people experiencing drying of $\geq 1/2\sigma_{TWS}$, which is roughly equivalent to a mean shift to abnormally dry conditions¹⁰ (Fig. 5b). Key regional impacts include intensified drying in Amazonia, a reversal of wetting in Southeast Asia and boreal drying that could counteract projected precipitation increases. Beyond water availability concerns, these changes may influence carbon-cycle and

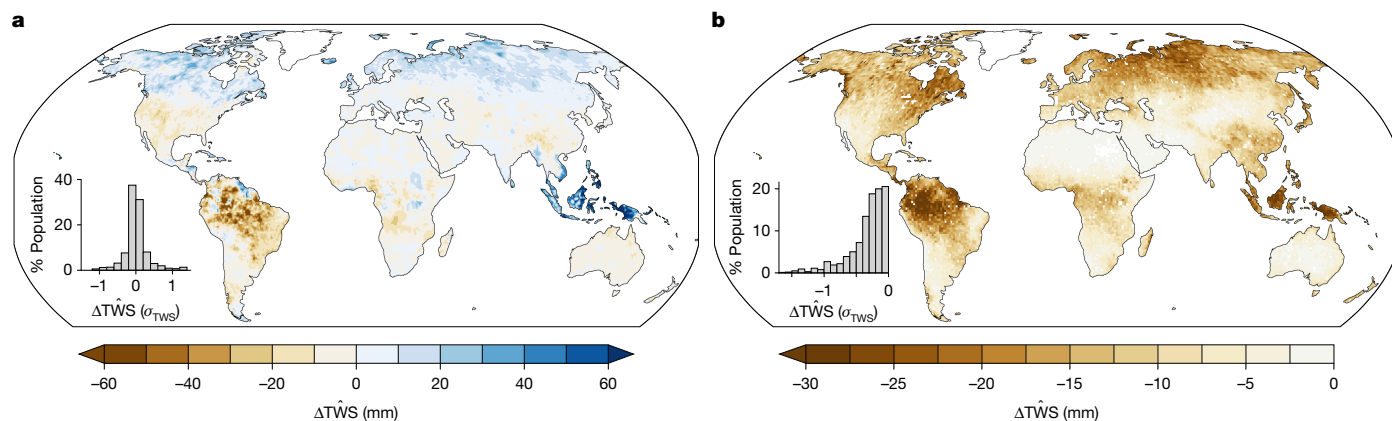


Fig. 5 | Historical and projected future impacts of precipitation concentration on TWS. a, Estimated TWS change inferred from G_p trends and the historical dependence of G_p on TWS, averaged across the CPC, GPCP and GPCC (refs. 21–23) precipitation datasets and expressed as total change over 1980–2022. **b,** Future TWS change from precipitation concentration under an

additional 1°C of warming beyond present, projected based on a simply thermodynamic precipitation intensification model forced by local mean annual warming. In **a, b**, the inset histograms show global population exposure to standardized TWS changes. Base map adapted from Natural Earth (<https://www.naturalearthdata.com>).

land-atmosphere feedbacks governing climate responses to greenhouse forcing^{29,35}.

Discussion

Debates over future terrestrial water availability have generally focused on projected long-term changes in mean total precipitation and evaporation. Our findings advance this framework by showing that the character of the daily precipitation distribution itself exerts a first-order influence on TWS, independent of total precipitation. The concentration effect—encompassing both radiative and hydrologic partitioning changes—reduces the water retained on land almost as much as total precipitation increases it. These results reframe aridity beyond cumulative fluxes, highlighting the role of land-surface processes and their interaction with warming-induced precipitation concentration in integrating daily precipitation variability.

The drying effect of precipitation concentration arises primarily from increased evaporative losses, as shown in both observations and land model simulations. Intense precipitation can exceed soil infiltration capacity, accumulating at the surface where lower aerodynamic resistance increases evaporation, particularly during longer and sunnier dry periods. Enhanced evaporation explains why higher- G_p years are not warmer (Fig. 1e) despite increased shortwave radiation (Fig. 3a). Although shortwave radiation anomalies contribute to enhanced evaporation, the temporal distribution of daily precipitation largely explains the drying effect of concentration. Further clarity on the nature of evaporation responses to precipitation concentration may be obtained in future research through further analysis of sub-annual timescales and in situ observations from flux towers (Supplementary Fig. 2), soil moisture probes and gauged catchments.

Despite increased surface ponding, our results show no significant total runoff response to precipitation concentration. This contrasts with basin-scale studies, and is probably due to differences in scale and how hydrologic budget terms are classified. For example, some models count ponded water as surface runoff, whereas our approach considers it a distinct internal water flux, one that preferentially evaporates before export downstream^{36,37} (Fig. 4b,c, Methods and Extended Data Fig. 7). In arid regions, inconsistencies between empirical and modelled evaporation responses suggest unresolved complexities in dryland hydrology, warranting further investigation. Nevertheless, our results point to the importance of overland flow and its associated evaporation for TWS variability in the context of hydrologic intensification, challenging prevailing hydrologic theory^{38,39}.

The global TWS effect that we identify seems to be an intrinsic feature of the physical climate system that is also amplified by feedbacks from human irrigation water use. More concentrated precipitation dries the land most strongly in intensively irrigated areas (about 5% of land area in our sample; Extended Data Fig. 6a), including the North China and Gangetic Plains and the Mississippi and Nile Deltas. At the same time, the global TWS effect is observed over land areas with little or no irrigation (about 95% of our sample; Extended Data Fig. 6a), indicating that it is an independent effect borne of land-atmosphere dynamics. Where this physical effect occurs over heavily irrigated areas, it intensifies irrigation water use, further depleting TWS locally.

Collectively, our results indicate that precipitation concentration shapes long-term hydrologic trends, but several important areas for work remain. First, our water-year scale analysis does not account for snow and ice, despite their important role in seasonal water storage and potential concentration of snowfall under warming^{40,41}. Second, although soil characteristics and land-use changes likely modulate precipitation partitioning across regions, our analysis can only control for their aggregate impacts using fixed effects because of limited observations⁴². Complex land-surface models run with varying land use and land cover changes could help explain how such boundary conditions shape the TWS response. Third, although intense rainfall events or flooding can recharge groundwater⁴³, our results can only indicate that these gains are insufficient to offset increased evaporative losses, or localized to a few specific basins (Fig. 2c). Fourth, we do not separate transpiration from evaporation, but vegetation responses to the radiative and partitioning facets of precipitation concentration probably contribute to the TWS effect^{20,44–46}. Finally, future analyses should explore how the seasonality and surface moisture memory of concentration influence TWS responses to G_p (refs. 47,48). Although antecedent dry conditions increase soil storage, they can also induce hydrophobicity that limits infiltration. That we detect a consistent TWS response without an explicit antecedent soil moisture control suggests that, on average, more concentrated precipitation reduces TWS regardless of previous moisture conditions. Any influence of antecedent moisture is probably picked up by our temperature and precipitation controls or is comparatively small.

We show that precipitation concentration has already influenced TWS trends, notwithstanding the continued impact of total annual precipitation variability⁴⁹. As concentration increases nonlinearly with continued warming, its effect on TWS is likely to become larger and more negative in the future, weighing the scales towards drying irrespective of local changes in annual precipitation. Although the sign

of forced annual precipitation changes remains uncertain over many land areas, precipitation concentration consistently increases with warming, and its effect on TWS is ubiquitously negative. Our results may thus serve as a new basis for reducing uncertainty in land water availability projections, beyond a reliance on uncertain long-term precipitation changes⁵⁰.

At present, the theories of hydrologic response to climate change do not adequately capture the links we identify between the daily precipitation distribution, shortwave radiation, evaporation and the land water balance. Precipitation concentration arises from the differing responses of daily and annual precipitation to warming. Consequently, changes in dry day frequency, precipitation intensity and solar radiation are inherently coupled by cloud and land-atmosphere feedbacks, and jointly shape the surface supply of and atmospheric demand for evaporable water. A more complete theory would integrate these land-atmosphere processes alongside the long-term precipitation–evaporation balance. Our study provides an observational basis for such a theory, which could serve as a valuable counterbalance to the growing complexity and decreasing interpretability of Earth system models¹¹.

Online content

Any methods, additional references, Nature Portfolio reporting summaries, source data, extended data, supplementary information, acknowledgements, peer review information; details of author contributions and competing interests; and statements of data and code availability are available at <https://doi.org/10.1038/s41586-026-10487-7>.

1. Green, J. K. et al. Large influence of soil moisture on long-term terrestrial carbon uptake. *Nature* **565**, 476–479 (2019).
2. Proctor, J., Rigden, A., Chan, D. & Huybers, P. More accurate specification of water supply shows its importance for global crop production. *Nat Food* **3**, 753–763 (2022).
3. Roderick, M. L., Greve, P. & Farquhar, G. D. On the assessment of aridity with changes in atmospheric CO₂. *Water Resour. Res.* **51**, 5450–5463 (2015).
4. Held, I. M. & Soden, B. J. Robust responses of the hydrological cycle to global warming. *J. Clim.* **19**, 5686–5699 (2006).
5. Dai, A., Rasmussen, R. M., Liu, C., Ikeda, K. & Prein, A. F. A new mechanism for warm-season precipitation response to global warming based on convection-permitting simulations. *Clim. Dyn.* **55**, 343–368 (2020).
6. Douville, H., Chadwick, R., Sainit-Lu, M. & Medeiros, B. Drivers of dry day sensitivity to increased CO₂. *Geophys. Res. Lett.* **50**, e2023GL103200 (2023).
7. Petrova, I. Y. et al. Observation-constrained projections reveal longer-than-expected dry spells. *Nature* **633**, 594–600 (2024).
8. Allan, R. P. et al. Advances in understanding large-scale responses of the water cycle to climate change. *Ann. N. Y. Acad. Sci.* **1472**, 49–75 (2020).
9. Wainwright, C. M., Allan, R. P. & Black, E. Consistent trends in dry spell length in recent observations and future projections. *Geophys. Res. Lett.* **49**, e2021GL097231 (2022).
10. Zhao, M., A. G., Velicogna, I. & Kimball, J. S. A global gridded dataset of GRACE drought severity index for 2002–14: comparison with PDSI and SPEI and a case study of the Australia millennium drought. *J. Hydrometeorol.* **18**, 2117–2129 (2017).
11. Byrne, M. P. et al. Theory and the future of land-climate science. *Nat. Geosci.* **17**, 1079–1086 (2024).
12. Hegerl, G. C. et al. Challenges in quantifying changes in the global water cycle. *Bull. Am. Meteorol. Soc.* **96**, 1097–1115 (2015).
13. Pendergrass, A. G. & Knutti, R. The uneven nature of daily precipitation and its change. *Geophys. Res. Lett.* **45**, 11,980–11,988 (2018).
14. Allen, M. R. & Ingram, W. J. Constraints on future changes in climate and the hydrologic cycle. *Nature* **419**, 224–232 (2002).
15. Byrne, M. P. & Schneider, T. Narrowing of the ITCZ in a warming climate: physical mechanisms. *Geophys. Res. Lett.* **43**, 11,350–11,357 (2016).
16. Benestad, R. E. Implications of a decrease in the precipitation area for the past and the future. *Environ. Res. Lett.* **13**, 044022 (2018).
17. Sharma, A., Wasko, C. & Lettenmaier, D. P. If precipitation extremes are increasing, why aren't floods? *Water Resour. Res.* **54**, 8545–8551 (2018).
18. Tabari, H. Climate change impact on flood and extreme precipitation increases with water availability. *Sci. Rep.* **10**, 13768 (2020).
19. Slette, I. J., Blair, J. M., Fay, P. A., Smith, M. D. & Knapp, A. K. Effects of compounded precipitation pattern intensification and drought occur belowground in a mesic grassland. *Ecosyst.* **25**, 1265–1278 (2022).
20. Feldman, A. F. et al. Large global-scale vegetation sensitivity to daily rainfall variability. *Nature* **636**, 380–384 (2024).
21. Adler, R. F. et al. The version-2 Global Precipitation Climatology Project (GPCP) monthly precipitation analysis (1979–present). *J. Hydrometeorol.* **4**, 1147–1167 (2003).
22. Chen, M. et al. Assessing objective techniques for gauge-based analyses of global daily precipitation. *J. Geophys. Res. Atmos.* **113**, D04110 (2008).
23. Schamm, K. et al. Global gridded precipitation over land: a description of the new GPCP First Guess Daily product. *Earth Syst. Sci. Data* **6**, 49–60 (2014).

24. Tapley, B. D., Bettadpur, S., Watkins, M. & Reigber, C. The gravity recovery and climate experiment: mission overview and early results. *Geophys. Res. Lett.* **31**, L09607 (2004).
25. Save, H., Bettadpur, S. & Tapley, B. D. High-resolution CSR GRACE RLO5 mascons. *J. Geophys. Res. Solid Earth* **121**, 7547–7569 (2016).
26. Tapley, B. D. et al. Contributions of GRACE to understanding climate change. *Nat. Clim. Change* **9**, 358–369 (2019).
27. Pokhrel, Y. et al. Global terrestrial water storage and drought severity under climate change. *Nat. Clim. Change* **11**, 226–233 (2021).
28. Geruo, A., Velicogna, I., Kimball, J. S. & Kim, Y. Impact of changes in GRACE derived terrestrial water storage on vegetation growth in Eurasia. *Environ. Res. Lett.* **10**, 124024 (2015).
29. Humphrey, V. et al. Sensitivity of atmospheric CO₂ growth rate to observed changes in terrestrial water storage. *Nature* **560**, 628–631 (2018).
30. Fasullo, J. T., Lawrence, D. M. & Swenson, S. C. Are GRACE-era terrestrial water trends driven by anthropogenic climate change? *Advan. Meteorol.* **2016**, 4830603 (2016).
31. Rodell, M. et al. Emerging trends in global freshwater availability. *Nature* **557**, 651–659 (2018).
32. Wan, H., Zhang, X., Zwiers, F. & Min, S.-K. Attributing northern high-latitude precipitation change over the period 1966–2005 to human influence. *Clim. Dyn.* **45**, 1713–1726 (2015).
33. Seneviratne, S. I. et al. Investigating soil moisture–climate interactions in a changing climate: a review. *Earth Sci. Rev.* **99**, 125–161 (2010).
34. Budyko, M. I. & Miller, D. H. (eds) *Climate and Life* (Academic Press, 1974).
35. Andersen, O. B., Seneviratne, S. I., Hinderer, J. & Viterbo, P. GRACE-derived terrestrial water storage depletion associated with the 2003 European heat wave. *Geophys. Res. Lett.* **32**, L18405 (2005).
36. Blöschl, G. & Sivapalan, M. Scale issues in hydrological modelling: a review. *Hydrol. Process.* **9**, 251–290 (1995).
37. Beven, K. The era of infiltration. *Hydrol. Earth Syst. Sci.* **25**, 851–866 (2021).
38. Kirkby, M. Hillslope runoff processes and models. *J. Hydrol.* **100**, 315–339 (1988).
39. Jasechko, S., Kirchner, J. W., Welker, J. M. & McDonnell, J. J. Substantial proportion of global streamflow less than three months old. *Nat. Geosci.* **9**, 126–129 (2016).
40. Gottlieb, A. R. & Mankin, J. S. Observing, measuring, and assessing the consequences of snow drought. *Bull. Am. Meteorol. Soc.* **103**, E1041–E1060 (2022).
41. O’Gorman, P. A. Contrasting responses of mean and extreme snowfall to climate change. *Nature* **512**, 416–418 (2014).
42. Vereecken, H. et al. Soil hydrology in the Earth system. *Nat. Rev. Earth Environ.* **3**, 573–587 (2022).
43. Jasechko, S. & Taylor, R. G. Intensive rainfall recharges tropical groundwaters. *Environ. Res. Lett.* **10**, 124015 (2015).
44. Mankin, J. S., Seager, R., Smerdon, J. E., Cook, B. I. & Williams, A. P. Mid-latitude freshwater availability reduced by projected vegetation responses to climate change. *Nat. Geosci.* **12**, 983–988 (2019).
45. Lesk, C., Coffel, E. & Horton, R. Net benefits to US soy and maize yields from intensifying hourly rainfall. *Nat. Clim. Change* **10**, 819–822 (2020).
46. Lesk, C. S., Winter, J. M. & Mankin, J. S. Projected runoff declines from plant physiological effects on precipitation. *Nat. Water* **3**, 167–177 (2025).
47. Peterson, T. J., Saft, M., Peel, M. C. & John, A. Watersheds may not recover from drought. *Science* **372**, 745–749 (2021).
48. Berghuijs, W. R., Woods, R. A., Anderson, B. J., Hemshorn de Sánchez, A. L. & Hrachowitz, M. Annual memory in the terrestrial water cycle. *Hydrol. Earth Syst. Sci.* **29**, 1319–1333 (2025).
49. Rodell, M. & Li, B. Changing intensity of hydroclimatic extreme events revealed by GRACE and GRACE-FO. *Nat. Water* **1**, 241–248 (2023).
50. Ukkola, A. M., De Kauwe, M. G., Roderick, M. L., Abramowitz, G. & Pitman, A. J. Robust future changes in meteorological drought in CMIP6 projections despite uncertainty in precipitation. *Geophys. Res. Lett.* **47**, e2020GL087820 (2020).
51. Lehner, B. & Grill, G. Global river hydrography and network routing: baseline data and new approaches to study the world’s large river systems. *Hydrol. Process.* **27**, 2171–2186 (2013).
52. Cox, S. J., Stackhouse, P. W. Jr, Gupta, S. K., Mikovitz, J. C. & Zhang, T. NASA/GEWEX shortwave surface radiation budget: integrated data product with reprocessed radiance, cloud, and meteorology inputs, and new surface albedo treatment. *AIP Conf. Proc.* **1810**, 090001 (2017).
53. Kato, S. et al. Surface irradiances of edition 4.0 Clouds and the Earth’s Radiant Energy System (CERES) Energy Balanced and Filled (EBAF) data product. *J. Clim.* **31**, 4501–4527 (2018).
54. Martens, B. et al. GLEAM v3: satellite-based global land evaporation and root-zone soil moisture. *Geosci. Model Dev.* **10**, 1903–1925 (2017).
55. van den Hurk, B. et al. LS3MIP (v1.0) contribution to CMIP6: the Land Surface, Snow and Soil moisture Model Intercomparison Project – aims, setup and expected outcome. *Geosci. Model Dev.* **9**, 2809–2832 (2016).

Publisher’s note Springer Nature remains neutral with regard to jurisdictional claims in published maps and institutional affiliations.



Open Access This article is licensed under a Creative Commons Attribution-NonCommercial-NoDerivatives 4.0 International License, which permits any non-commercial use, sharing, distribution and reproduction in any medium or format, as long as you give appropriate credit to the original author(s) and the source, provide a link to the Creative Commons licence, and indicate if you modified the licensed material. You do not have permission under this licence to share adapted material derived from this article or parts of it. The images or other third party material in this article are included in the article’s Creative Commons licence, unless indicated otherwise in a credit line to the material. If material is not included in the article’s Creative Commons licence and your intended use is not permitted by statutory regulation or exceeds the permitted use, you will need to obtain permission directly from the copyright holder. To view a copy of this licence, visit <http://creativecommons.org/licenses/by-nc-nd/4.0/>.

© The Author(s) 2026

Methods

Data

TWS data come from the GRACE and GRACE-FO mass concentration solutions (RL06) developed by the Center for Space Research at the University of Texas²⁵. The dataset represents monthly total water mass variations (expressed as equivalent water height) at a gridded resolution of 0.25°. We omit data before August 2002 (due to sensor calibration at the outset of the GRACE mission) and for water-year 2017 (due to incomplete data during the mission gap between GRACE and GRACE-FO). We use GRACE TWS because it is an observational data product that holistically measures land water, capturing all surface and underground stocks.

To account for observational uncertainty, we use three daily gridded precipitation data products: the Global Precipitation Climatology Project (GPCP) Daily Precipitation Analysis v.1.3 (ref. 21), the Global Precipitation Climatology Center (GPCC) Daily Analysis v.2022 (ref. 23) and the National Oceanic and Atmospheric Administration Climate Prediction Center (CPC) Unified Gauge-Based Analysis²². GPCC is a station-based product (1° resolution) with coverage over 1982–2020, whereas CPC (0.5°) and GPCP (1°) integrate station and satellite observations over 1979–2022 and 1997–2022, respectively. We repeated our analysis for the more recent GPCP v.3.3 and find consistent main effects⁵⁶ (Supplementary Fig. 4), but use the more complete earlier version for our main analysis (GPCP v.3.3 contains missing daily values at high latitudes after 2020).

We use two net all-sky surface shortwave radiation datasets: the Global Energy and Water Exchanges Surface Radiation Budget (GEWEX-SRB, limited here to 2002–2017)⁵² daily dataset and the NASA Clouds and the Earth's Radiant Energy System Energy Balanced and Filled monthly dataset (NASA-EBAF, limited here to 2002–2022)⁵³, each at 1° resolution. We use monthly evapotranspiration from the GLEAM v.3.8a, at 0.25° resolution for the overlapping GRACE period (2002–2020; ref. 54). Main river basin boundaries are from the HydroBASINS v.1.0 dataset, which is derived from Shuttle Radar Topography Mission elevation data collected in 2000 (ref. 51). All data URLs are enumerated in Supplementary Table 1.

Daily climate model data are from the land-hist experiment of the Coupled Model Intercomparison Project, Phase 6, Land-Surface, Snow and Soil Moisture Intercomparison Project (CMIP6-LS3MIP)⁵⁵. In the land-hist experiment, the land-surface components of climate models are forced by atmospheric forcings from the Global Soil Wetness Project phase 3, whose precipitation data are derived from the NOAA-CIRES-DOE Twentieth Century Reanalysis (20CR). We include results from the two models that report all required variables: MIROC6 with land component MATSIRO and VISIT-e⁵⁷, and CNRM-CM6-1 with land component ISBA-CTRIP⁵⁸. We use the mrtws (total water storage), tas (mean surface air temperature) and pr (precipitation rate) variables. No participating models report these required variables plus evaporation, precluding extending our climate model analysis towards mechanisms.

Data aggregation and precipitation Gini coefficient

All data are temporally aggregated to the water-year scale, using October to September for the Northern Hemisphere water-year and July to June in the Southern Hemisphere. On this water-year scale, snow and ice storage changes are negligible. We further limit our spatial domain to regions without permanent snow and ice accumulation. We compute daily mean temperature data using the average of daily maximum and minimum temperatures from CPC. We also compute climatological mean precipitation as the average of the annual total over the full precipitation data record.

We linearly detrend GRACE data to isolate interannual variability, which is largely governed by hydroclimate variability, from long-term trends that include anthropogenic water use and management^{26,31}. The rationale for this focus on interannual variability is to establish whether more concentrated daily precipitation distributions lead to

cumulative water balance changes, averaged across the water-year, absent the influence of coincident economic, demographic and mean warming trends.

Correspondingly, and because GRACE only estimates TWS relative anomalies, we detrend and demean all other hydroclimate variables (except climatological precipitation, which is time-invariant). Finally, we interpolate all datasets to a common 0.5° grid as a compromise across the resolutions of the datasets. We repeated our analyses at alternative coarser common resolutions (1°, 2° and 3°) and found consistent results (Supplementary Fig. 5). We present long-term linear trends in terms of changes per 20 years to ease interpretation.

To quantify the annual concentration of daily precipitation, we apply the Gini coefficient, a common economic measure of income inequality⁵⁹, to the three daily precipitation datasets. The Gini coefficient is based on the Lorenz curve, which plots the cumulative share of the total quantity (that is, cumulative share of annual precipitation) against the cumulative share of the population (that is, days per year), sorted from least to greatest (Fig. 1d). The Gini coefficient is defined as the area between the Lorenz curve and the 1:1 line of equality. For more concentrated distributions, such as all of the annual precipitation falling in 1 day, the Lorenz curve deviates further from the line of equality, giving a Gini coefficient closer to 1. If all days are equally rainy, the Gini yields a value of 0. We use a computationally efficient discrete formulation to calculate the annual Gini coefficient of sorted daily precipitation (G_p):

$$G_p = \frac{1}{n} \left(n + 1 - 2 \frac{\sum_i^k \sum_i^n P_i}{\sum_i^n P_i} \right) \quad (1)$$

where n is the number of days per year and P is a sorted vector of precipitation values for a given water-year and location. The cumulative sum of P approximates the Lorenz curve (inner numerator double summation), and the normalized integral of that curve is estimated by summing the cumulative values (outer numerator double summation) and dividing by the total sum (denominator summation). This formulation is analytically identical to more common Gini formulations, but is computationally faster. As with the other variables, we linearly detrend and demean G_p to isolate local interannual anomalies.

G_p is—by formulation—sensitive to both incremental dry days and precipitation extremes. These joint sensitivities are mathematically coupled: in normalized terms, incremental dry days necessitate a greater concentration of annual precipitation into the remaining wet days, whereas incremental precipitation extremes leave less annual precipitation to be distributed across the remaining days of the year. This coupling maps conceptually with expectations from the physics of hydrologic intensification, in which daily precipitation responds more to warming than its annual total. We confirm this joint sensitivity of G_p by regressing its annual anomalies on annual occurrence of extreme precipitation days (>99th percentile of nonzero precipitation days), dry days (<0.1 mm), and total annual precipitation as well as on annual mean temperature.

Statistical models of TWS effect

For each precipitation dataset, the data aggregation and G_p calculations yield a panel of annual anomalies in TWS, mean temperature (T), total precipitation (P) and G_p , plus long-term (absolute) climatological mean precipitation (\bar{P}). The three panels vary in sample size because of differing time availability of the precipitation datasets (Supplementary Table 2).

To assess the influence of G_p on TWS for each panel, we apply linear fixed-effects models, a type of panel regression that enables controlling for time-invariant unobserved spatial heterogeneity using spatial fixed effects, as well as global shocks in any year using time fixed effects⁶⁰. Our approach minimizes confounding by spatial or temporal trends in environmental, climate or anthropogenic factors that may covary with G_p , without explicit inclusion in the model. Spatial fixed effects remove all static differences across grid cells, such as baseline differences in

soils, hydrogeology, vegetation and groundwater use or irrigation infrastructure. Water-year fixed effects absorb global shocks that affect all regions simultaneously (notably, El Niño events). By detrending all variables, we also exclude long-term groundwater depletion trends, ensuring that the model captures only interannual variability.

This identification strategy isolates the emergent interannual influence of precipitation concentration on TWS. The models are of the form

$$\text{TWS}^{i,t} = \theta T^{i,t} + \pi P^{i,t} + \gamma G_p^{i,t} + \chi G_p^{i,t} \bar{P}^i + \sigma^i + \tau^t + \varepsilon^{i,t} \quad (2)$$

where θ and π are coefficients of temperature and annual precipitation, σ and τ are spatial and time fixed effects, superscripts i and t denote grid cell and water-year, and ε is the residual. These terms are included as controls for the influence of other hydroclimate or unobserved variables. We estimate the effect of G_p as an interaction with climatological mean precipitation (using linear coefficient γ and interaction coefficient χ) to explicitly assess variation in the effect across the global aridity gradient. As such, the marginal effect of an anomaly ΔG_p on TWS is conditional on climatological precipitation and is given by

$$\Delta \text{TWS} = (\gamma + \chi \bar{P}) \Delta G_p \quad (3)$$

We interpret this marginal effect as the generalizable response of local interannual TWS variation to local anomalies of precipitation concentration, conditioned on local climatological wetness. We present the marginal effect of G_p on TWS per a 10 percentage-point change in G_p (that is, a G_p anomaly of 0.1) as G_p values are bounded between 0 and 1, and vary interannually by a smaller portion of that range. For each precipitation dataset, we estimate the coefficients in equation (2) separately using absolute anomalies (to quantify the effect in hydrologically meaningful units) and standardized anomalies (to enable comparison of effect sizes across predictors). Coefficients are estimated using the lfe package in R. Global Pearson correlation among predictors (pooled across space and time) is under 0.5 (r^2 under 0.25), indicating little scope for influence of collinearity on regression estimates (Extended Data Fig. 10). To ease visualization of standardized coefficients, we present the conditional G_p effect at the global population-weighted climatological mean precipitation value of 1,000 mm.

As the marginal effect of G_p on TWS is conditioned on climatological precipitation, its standard error depends on the variance of coefficients χ and γ as well as the climatological precipitation. We estimate this standard error (SE) using the variance of linear combinations of estimators:

$$\text{SE}(\gamma + \chi \bar{P}) = \sqrt{\text{var}(\gamma) + \bar{P}^2 \text{var}(\chi) + 2\bar{P} \cdot \text{cov}(\gamma, \chi)} \quad (4)$$

When estimating the variances and covariance of χ and γ , we cluster standard errors at the main river basin scale to account for spatial and temporal autocorrelation of gridded data⁵¹—this step yields more conservative standard errors and avoids type-I errors due to the non-independence of observations. We also tested Conley spatial standard errors⁶¹ with distance cutoffs of 300 km (roughly the effective resolution of GRACE) and 750 km (the average length scale of global river basins in HydroSHEDS; Supplementary Fig. 6a–c), and Driscoll–Kraay temporal standard errors with time cutoffs of 3 years and 5 years (Supplementary Fig. 6d–f). All approaches yield similar confidence intervals. At a given value of climatological precipitation, we consider the marginal effect of G_p on TWS as statistically significant, for which its median estimate plus or minus two standard errors excludes zero.

We also estimate a reduced form of equation (2) at the main river basin scale to check the robustness of the global effect at finer spatial scales⁵¹, and to characterize its spatial variability. We omit the interaction between G_p and climatological precipitation, as variation in climatological precipitation within basins is smaller than across the globe. For simplicity, we present these basin-scale TWS effects as the average across the three products, wherever they are significant ($P < 0.05$) and

of consistent sign in at least two of the three precipitation data products. Basin-scale TWS effects are fairly consistent across the three data products (Extended Data Fig. 5).

Although spatial fixed effects control for time-invariant spatial differences, they do not control for confounders that vary interannually in response to G_p itself, such as irrigation responses to year-to-year variation in TWS change, which might deplete groundwater. To isolate the influence of irrigation, we add an interaction term, I , for the grid cell area equipped for irrigation to equation (2) (using data from the UN Food and Agriculture AQUASTAT Global Information System on Water and Agriculture):

$$\text{TWS}^{i,t} = \theta T^{i,t} + \pi P^{i,t} + \gamma G_p^{i,t} + \chi G_p^{i,t} \bar{P}^i + \varphi G_p^{i,t} I^i + \delta I^i G_p^{i,t} \bar{P}^i + \sigma^i + \tau^t + \varepsilon^{i,t} \quad (5)$$

In this model, the influence of G_p on TWS depends on both climatological mean precipitation and irrigation area, which we evaluate at varying levels. The approach enables our isolation of irrigation influence, despite 95% of grid cells in our analysis containing <1% irrigated area.

For the CMIP6-LS3MIP land-hist climate model data, we apply the identical data aggregation and statistical modelling in equations (2–4) to the simulated TWS, T , P and G_p . To test the robustness of the estimated TWS effect to temporal and spatial variability in gauge coverage, we regress the basin-level TWS effects on the on basin mean areal gauge density (gauges per basin) and on the coefficient of variation of the number of gauges per basin over time (standard deviation of gauges per basin divided by the average), based on the GPCC gauge count data. The relationships show no significant dependence of the basin-level TWS effect on areal station density or the degree of year-to-year variation in gauge density (Extended Data Fig. 6b,c). Empirical results using only GRACE (through water 2016) and excluding GRACE-FO (2018–2022) are consistent with those using the complete GRACE record⁶² (Supplementary Table 3).

Statistical models of effect mechanism

To clarify the mechanism of the effect of G_p on TWS, we develop two companion panel regressions similar to those used to assess the TWS effect, but using GLEAM evapotranspiration (E) and shortwave radiation (S) anomalies from GEWEX-SRB and NASA EBAF in place of TWS in equation (2). To isolate the intensity-partitioning mechanism of the TWS effect, we add a regressor in the form of shortwave radiation anomalies in equation (2) to explicitly control for the radiative effect of additional dry days:

$$\text{TWS}^{i,t} = \theta' T^{i,t} + \pi' P^{i,t} + \gamma' G_p^{i,t} + \chi' G_p^{i,t} \bar{P}^i + \zeta S^{i,t} + \psi S^{i,t} \bar{P}^i + \sigma'^i + \tau'^t + \varepsilon'^{i,t} \quad (6)$$

We model the effect of S on TWS, including an interaction with climatological precipitation to account for variable effects across gradients of mean aridity (and thus energy compared with moisture limitation). As such, ζ is the TWS sensitivity to shortwave radiation anomalies and ψ is the interaction effect with mean precipitation. The prime symbols indicate coefficients estimated with the S control, to distinguish from coefficients in equation (2).

Introducing the S control removes the TWS variance attributable to shortwave anomalies, which are positively correlated with G_p , from the estimated G_p effect. We consider this positive S – G_p correlation as a facet of the hydrologic effects of precipitation concentration, so we omit this control when estimating the full TWS effect. However, we include the S control in equation (6) to isolate the land-surface hydrologic partitioning effects of daily precipitation distribution on TWS, apart from the fact that more concentrated precipitation years are sunnier. We interpret this isolated effect as the influence of more intense precipitation on surface partitioning, such as infiltration-excess or saturation-excess ponding of precipitation on the surface.

For simplicity, we present this partitioning effect as an average of effects across the three precipitation datasets, with uncertainty characterized as the maximum and minimum of the full two standard error interval across the three precipitation and two radiation data products. This approach is conservative, as standard errors would be smaller if we first averaged the precipitation data, rather than averaging effects. However, results for individual datasets are consistent with those from the three-product average (Supplementary Fig. 1). To estimate the relative fractional contribution of the partitioning effect to the full effect (f_b), we divide the partitioning effect by the marginal effect estimated using equations (2) and (3):

$$f_b = \frac{y' + \chi' \bar{P}}{y + \chi \bar{P}} \quad (7)$$

Because it is simpler to visualize, we present this fractional distribution effect both for the average across data products and for each individual product (based on the data in Supplementary Fig. 1).

Reanalysis models contain appreciable biases in the simulation of daily precipitation, especially for extreme values that contribute disproportionately to annual precipitation and strongly influence concentration⁶³. As such, we favour an empirical approach based on observational hydroclimate and TWS data. But understanding the mechanism of the observed effect requires assessing surface water budget terms that are poorly observed globally. We use GLEAM evapotranspiration data to establish the plausibility of evapotranspiration responses to G_p . But as GLEAM assimilates precipitation data (and thus biases) from reanalysis, it probably underrepresents daily precipitation concentration effects. We similarly use the FLUXCOM CERES-GPCP flux-tower based energy and water flux dataset (2001–2014) to provide an in situ window on evaporative responses to precipitation concentration⁶⁴; however, as its observational constraint is limited to the approximately 100 m radius surrounding the tower, these data are not comparable to GLEAM, estimated on a 0.25° grid. To overcome these observational limitations on water-budget terms (evaporation and runoff), we extend a simple, process-based land–atmosphere model with hydrology⁶⁵, driven by the daily precipitation datasets at a set of grid points sampling the global precipitation gradient.

Idealized land-surface model

We use an idealized process-based land-surface model to provide additional evidence for the negative TWS effect of G_p and to clarify its mechanism (the underlying surface water balance changes and their drivers). Although more complex land-surface contain more complete process representations, the ultimate energy–moisture balance rests on nested and coupled parameterizations, making a mechanistic diagnosis difficult, if not impossible.

Embracing recent community calls for robust and simple theories of land surface climate¹¹, we run land-surface model simulations that parsimoniously capture variations in surface precipitation partitioning and land–atmosphere coupling. We use experimental design that enables direct comparison with the observed TWS effect. First, as the observed TWS effect is due to G_p anomalies and because GRACE TWS measures anomalies, we focus on simulating the sensitivity of TWS to changes in G_p , rather than mean TWS itself. Second, our statistical model includes space fixed effects to capture time-invariant differences in land cover and soil characteristics. Our idealized model mirrors this approach by using median parameters globally, rather than calibrating parameters locally. In short, rather than developing and validating a complete and realistic model of all of the processes driving TWS, we develop the minimal physics required to plausibly explain our observational results and assess the most important underlying processes.

Our process-based model parsimoniously represents the coupled surface partitioning of precipitation and energy–moisture balance. It extends the one-dimensional simple energy–moisture balance (SEMB)

model, developed in ref. 65, to represent precipitation partitioning at the land surface and simulate a surface water stock (Extended Data Figs. 9 and 10). In the original model formulation, precipitation infiltrated instantaneously into the soil moisture stock (M_s), irrespective of its intensity. On saturation, excess runoff was treated as an instantaneous water flux outside the model domain, precluding evaporation from surface water within the model. Our extended model (SEMB with hydrology, SEMB-H) includes intensity-dependent surface partitioning of precipitation towards infiltration compared with infiltration and saturation excess, the latter two being retained within the model using a surface water stock (M_l), whose outputs include evaporation and runoff. Physically, these developments allow the model to more completely represent surface precipitation partitioning processes: when precipitation meets the land, water can pool at the surface if the infiltration capacity of the soil or maximum saturation have been reached, and this ponded surface water can run off or evaporate.

The surface energy balance is given in terms of time-evolving surface air temperature (T) as

$$C \frac{dT}{dt} = F_{SW} - D - LE_s = F_{SW} - \alpha(T - \bar{T}_D) - \frac{L\rho_a M_s}{r_s} [q_{sat}(T) - \bar{q}] \quad (8)$$

where C is the effective heat capacity of the soil layer, F_{SW} is the net surface shortwave radiation, D is the sum of net longwave radiation and the ground and sensible heat fluxes (that is, the ‘dry’ energetic response), E_s is evaporation from soils and L is the enthalpy of vapourization of water. Following ref. 65, D is parameterized as a function of the dewpoint depression ($T - \bar{T}_D$) using a dry energetic parameter α , representing the temperature-damping efficiency of non-evaporative fluxes. We derive the value of α from ref. 65, estimated by regressing the sum of longwave, sensible heat and ground heat fluxes on the surface dewpoint depression temperature in ERA-Interim reanalysis. Evaporation is parameterized as a function of vapour pressure deficit ($q_{sat}(T) - \bar{q}$) by r_s , which is the bulk soil surface resistance (ρ_a is the mean density of air). Atmospheric humidity variables (\bar{q} and \bar{T}_D) are fixed to climatological mean values, as local variability in atmospheric evaporative demand is more strongly related to temperature than specific humidity variation. Evaporation is also a linear function M_s (that is, soil wetness), expressed in terms of saturation state.

The change in soil moisture stock is precipitation less soil evaporation, infiltration and saturation-excess ponding rate of water, and soil drainage. We simulate it as

$$\mu_s \frac{dM_s}{dt} = P - E_s - Q_s(P) - Q_D(M_s) \quad (9)$$

where P is daily precipitation, Q_s is ponded surface water (infiltration excess and surface excess), Q_D is soil drainage (also known as subsurface runoff in many land-surface models) and μ_s is a geometric parameter to convert between water equivalent heights and saturation state. Q_s is parameterized using the US Soil Conservation Service Curve Number scheme developed by the United States Department of Agriculture^{66–68}, which posits a quadratic increase in the surface ponding rate (saturation and infiltration excess) as a function of daily precipitation intensity and a parameter, S , that captures the maximal retention of soil water:

$$Q_s(P) = \frac{(P - \lambda S)^2}{P - (1 - \lambda)S} \quad (10)$$

$$S = 25.4 \left(\frac{1,000}{\text{CN}} - 10 \right) \quad (11)$$

In this parametrization, λ is a parameter representing the ratio between initial abstraction of precipitation and potential maximum

Article

soil water retention (S), which determines the minimum daily precipitation at which ponding occurs. Beyond this minimum, surface ponding rate increases according to the curve number (CN) parameter (a value between 0 and 100), which reflects the surface ponding rate sensitivity to precipitation intensity. We use CN values of 30 (dense forest cover), 50 (sparse woody vegetation on sandy loam soil) and 80 (grassland or impervious surfaces) in our model experiments⁶⁷. The soil drainage (or subsurface runoff term), Q_D , is parametrized in terms of unsaturated hydraulic conductivity:

$$Q_D(M_S) = k_{\text{sat}} M_S^c \quad (12)$$

where k_{sat} is the saturated hydraulic conductivity and c is parameter controlling the nonlinear response of soil water leakage to soil saturation states above the field capacity⁶⁹. Parameter values are for median sandy loam soils (Supplementary Table 3).

A key innovation in the model is to assess the potential for precipitation to pool on the land surface and evaporate before it contributes to total runoff. We model ponded surface water and soil drainage as contributing to the surface water stock (M_L), which is governed by

$$\mu_L \frac{dM_L}{dt} = P - E_L + Q_S(P) + Q_D(M_S) - Q_L(M_L) \quad (13)$$

where E_L is evaporation from the surface water stock, Q_L is runoff out of the surface water stock, and μ_L is a geometric parameter to convert between water equivalent heights and saturation state (that is, fractional ‘fullness’ of the reservoir). In our specification, Q_D , or soil drainage, contributes to surface water stocks, reflecting the dominant contribution of soil drainage to streamflow through subsurface flow^{70,71}. E_L is parametrized similarly to E_S , but as a function of M_L instead of M_S and with a lower bulk surface resistance (r_L). This lower resistance captures stomatal control on transpiration over land, and the fact that water evaporates more easily from a free surface (Supplementary Table 3). As our model stipulates a minority areal fraction covered by the surface water stock (10% in the median parameters; Supplementary Table 3), we assume that the temperature (and thus vapour pressure deficit) over surface water is dictated by the energy balance over soils. This simplification enables us to simulate E_L without simulating horizontal transfers within the atmosphere, but results are similar using a simple bulk temperature-homogenization scheme (Supplementary Fig. 7). Q_L is parametrized as a quadratic function of M_L and a maximum fractional daily outflow rate parameter (ω), such that $Q_L = \omega M_L^2$. In this formulation, runoff occurs only at the boundary of the model, enabling the model to track whether ponded surface water evaporates before leaving the grid cell. We use a global mean range of ω values based on the mean turnover rate of freshwater in lakes and reservoirs, estimated as the ratio of mean runoff ($5 \times 10^4 \text{ km}^3 \text{ yr}^{-1}$; ref. 72) to global total surface freshwater volume ($2 \times 10^5 \text{ km}^3$; ref. 73), or around 0.1% per day. We also run the model with larger ω values (0.5–1% per day) to account for the volumetric dominance of large, slowly overturning lakes.

We initialize our model at a surface air temperature of 280 K and with a saturation state of 0.5 for the soil and surface water stocks. In contrast to more complex land-surface models featuring deep soil water stocks, all prognostic variables are governed by fast first-order dynamics with characteristic e-folding times of the order of days, as defined by the geometry, parameters and forcings of the model. As such, we run our idealized model experiments without a multi-year spin-up common for complex land-surface models.

Land-surface model experimental design

To simulate the TWS effect using SEMB-H, we run the model using P and F_{sw} forcings from CPC and GEWEX-SRB at 1,400 points randomly sampled across the global range of climatological precipitation. At each location, we run the model twice, using forcings for the highest and

lowest G_p year available in the observational CPC data. This approach captures variation in both daily P and S and how they, in turn, shape G_p . To isolate the effect of G_p from that of annual precipitation, we scale the daily P time series from each of these two years to ensure that they have equal totals (Extended Data Fig. 8). This eliminates confounding TWS effects of low and high precipitation years, analogously to our control for annual precipitation in equation (2). We estimate the simulated TWS effect ($\Delta \text{TWS}_{\text{sim}}$) as the difference between maximum and minimum G_p years in volume-weighted sums of M_L and M_S . To match the water-year scale of our empirical analysis, we take this difference as an average across the water-year (denoted by overbars):

$$\Delta \text{TWS}_{\text{sim}} = \mu_S a_S (\overline{M_S|G_p^{\text{max}}} - \overline{M_S|G_p^{\text{min}}}) + \mu_L a_L (\overline{M_L|G_p^{\text{max}}} - \overline{M_L|G_p^{\text{min}}}) \quad (14)$$

where a_S and a_L are the areal fractions of soil compared with surface water stocks. As these simulated TWS responses reflect a wide range of actual G_p differences, we linearly scale $\Delta \text{TWS}_{\text{sim}}$ to a uniform $0.1 \Delta G_p$ as in our empirical analysis. Finally, we express the simulated TWS effect as a global statistical relationship in terms of climatological precipitation, for comparison to our empirical results:

$$\Delta \text{TWS}_{\text{sim}}^i = \beta_0 + \beta_1 \overline{P}^i + \varepsilon^i \quad (15)$$

where i denotes points in our sample. As we keep annual precipitation and surface parameters constant in our simulations, equation (15) is analogous to equation (2), such that β_0 and β_1 are the simulated equivalents of γ and χ . We estimate uncertainty in equation (15) analogously to in equation (4), and compare the confidence intervals of the empirical and simulated TWS effects. We also track the mean differences in water-year totals of E_L , E_S , Q_S and Q_L between the maximum and minimum G_p years to attribute the TWS effect to surface water budget changes. E_L reflects evaporation from ponded surface water as well as from initial moisture stocks, as E_L is initialized at 0.5 (that is, half full), and as such is not necessarily limited by Q_S .

The main free parameters in SEMB-H are the dry radiative coefficient (α), the CN, the fractional daily outflow rate from the surface water stock (ω) and the geometric parameters governing the potential height and fractional area of the soil and surface water stocks (h and a). To test the robustness of our simulation results to values of these free parameters, we rerun the simulations using 243 combinatoric parameter sets at the 1,400 points (a total of about 365,000 simulations; Supplementary Table 3), and compare the range of simulated TWS effects (equation (15)) to the confidence intervals of the empirical effect. We further characterize the relative influence of free parameter values on the simulated TWS effect using Sobol’s indices, a variance-based sensitivity analysis across the full parameter space⁷⁴. This analysis allows us to assess how uncertainty in each parameter, individually and jointly (through interactions), affects uncertainty in the simulated TWS effect.

Imputed TWS changes

Using the global coefficients from equation (2) and local climatological precipitation across global land area, we estimate the TWS impact of G_p trends ($\Delta \text{TWS}_{\text{hist}}$) over 1980–2022 using

$$\Delta \text{TWS}_{\text{hist}}^i = (\gamma + \chi \overline{P}^i) \Delta G_p^i \quad (16)$$

In this formulation, TWS impacts depend on climatological precipitation and concentration trends at a given grid cell (superscripts i). This approach assumes that TWS effects of concentration, as estimated from detrended interannual variability, operate similarly over multi-decadal trends. We present the imputed historical TWS impact as an average across data products for simplicity.

To project future TWS impacts of concentration under continued global warming, we first use a simple thermodynamic model to project daily precipitation distribution changes under mean warming across

global land⁴⁵. This model enables efficient and transparent estimates of future concentration globally, isolated from the influence of long-term annual precipitation changes and avoids consistent daily precipitation biases in general circulation models. The model intensifies observed daily precipitation distributions (I) at a fractional scaling rate of φ per degree of local warming (ΔT):

$$I' = (1 + \varphi)^{\Delta T} I \quad (17)$$

For φ , we use the Clausius–Clapeyron saturation vapour pressure sensitivity to temperature of $7\% \text{ } ^\circ\text{C}^{-1}$, drawing from observational literature linking daily precipitation intensity to temperature^{8,75}. Our goal is to briefly contextualize the TWS implications of median concentration expectations, so here we do not explore uncertainty in this parameter. For the initial observed intensity, I , we use daily precipitation distributions for the water-year with G_p closest to the long-term median. Precipitation intensification is projected at an illustrative $1 \text{ } ^\circ\text{C}$ of global mean surface air temperature warming beyond the study period (or about $2 \text{ } ^\circ\text{C}$ above the pre-industrial limit), in line with current plausible mitigation scenarios for the late-twenty-first century. The local surface air temperature warming pattern at $1 \text{ } ^\circ\text{C}$ of global mean warming is derived from the average of 26 CMIP6 models⁷⁶, run under the SSP5-8.5 scenario.

Annual precipitation generally changes by less than $7\% \text{ } ^\circ\text{C}^{-1}$, implying an increase in dry days. Consistent with our empirical model formulation, we enforce constant annual precipitation to isolate the influence of concentration changes under warming. To achieve this, we offset the increased precipitation from intensification by converting the lowest- M precipitation days to dry days, where M is the number of days for which the total precipitation equals the intensification-induced annual increase. We then difference the G_p of this final concentrated distribution from the G_p of the initial, observed distribution to estimate G_p changes under warming. These projected G_p changes are of similar order to historical trends (1–10 basis points; Fig. 1g and Extended Data Fig. 3).

Finally, we use this G_p -change field to project changes in TWS, as in equation (16). Apart from mapping local TWS impacts, we also estimate global population exposure to standardized mean TWS changes using population data from the Intersectoral Impact Model Intercomparison Project⁷⁷. We first project the TWS impacts onto the population data to derive a frequency distribution of exposure, then quantify the proportion of the global population experiencing standardized anomalies exceeding 0.5 standard deviations—an illustrative threshold indicative of abnormally dry conditions¹⁰. We simply provide a median estimate for these population exposure estimates as a first-order characterization of the global importance of these effects. Importantly, our approach assumes that spatial and temporal patterns of global irrigation remain constant in the future. Because intensively irrigated areas experience a stronger TWS effect from precipitation concentration (Extended Data Fig. 6a), expansion or intensification of irrigated areas could lead to locally stronger future drying. Conversely, improvements in irrigation efficiency may reduce withdrawals per unit area in response to precipitation concentration.

Data availability

All datasets supporting the findings of this study are freely available from the URLs listed in Supplementary Table 1. The derived datasets are freely available at Zenodo^{78,79} (<https://doi.org/10.5281/zenodo.19116027> and <https://doi.org/10.5281/zenodo.19191145>).

Code availability

All processing, analysis and visualization codes to reproduce the results and figures of this study are freely available at Zenodo^{78,79}

(<https://doi.org/10.5281/zenodo.19116027> and <https://doi.org/10.5281/zenodo.19191145>). All maps were produced using the Cartopy Python library v.0.18.0 (<https://scitools.org.uk/cartopy/docs/v0.18/>), which uses geographic features from Natural Earth (<https://www.natural-earthdata.com>).

56. Huffman, G. J. et al. The new version 3.2 Global Precipitation Climatology Project (GPCP) monthly and daily precipitation products. *J. Clim.* **36**, 7635–7655 (2023).
57. Tatebe, H. et al. Description and basic evaluation of simulated mean state, internal variability, and climate sensitivity in MIROC6. *Geosci. Model Dev.* **12**, 2727–2765 (2019).
58. Voldoire, A. et al. Evaluation of CMIP6 DECK experiments with CNRM-CM6-1. *J. Adv. Model Earth Syst.* **11**, 2177–2213 (2019).
59. Dorfman, R. A formula for the Gini coefficient. *Rev. Econ. Stat.* **61**, 146–149 (1979).
60. Angrist, J. D. & Pischke, J.-S. *Mostly Harmless Econometrics: An Empiricist's Companion* (Princeton Univ. Press, 2009).
61. Conley, T. G. GMM estimation with cross sectional dependence. *J. Econom.* **92**, 1–45 (1999).
62. Landerer, F. W. et al. Extending the global mass change data record: GRACE follow-on instrument and science data performance. *Geophys. Res. Lett.* **47**, e2020GL088306 (2020).
63. Nogueira, M. Inter-comparison of ERA-5, ERA-interim and GPCP rainfall over the last 40 years: process-based analysis of systematic and random differences. *J. Hydrol.* **583**, 124632 (2020).
64. Jung, M. et al. The FLUXCOM ensemble of global land-atmosphere energy fluxes. *Sci. Data* **6**, 74 (2019).
65. Zeppetello, L. R. V., Battisti, D. S. & Baker, M. B. The physics of heat waves: what causes extremely high summertime temperatures? *J. Clim.* **35**, 2231–2251 (2022).
66. Alves, G. J., de Mello, C. R., Beskow, S., Junqueira, J. A. & Nearing, M. A. Assessment of the soil conservation service—curve number method performance in a tropical oxisol watershed. *J. Soil Water Conserv.* **74**, 500–512 (2019).
67. HEC-RAS v.6.0 (US Army Corps of Engineers, 2021).
68. Bonan, G. *Ecological Climatology: Concepts and Applications* (Cambridge Univ. Press, 2016).
69. Rodríguez-Iturbe, I. & Porporato, A. *Ecohydrology of Water-Controlled Ecosystems: Soil Moisture and Plant Dynamics* (Cambridge Univ. Press, 2007).
70. Xie, J. et al. Majority of global river flow sustained by groundwater. *Nat. Geosci.* **17**, 770–777 (2024).
71. Alley, W. M., Healy, R. W., LaBaugh, J. W. & Reilly, T. E. Flow and storage in groundwater systems. *Science* **296**, 1985–1990 (2002).
72. Liang, S. & Greene, R. A high-resolution global runoff estimate based on GIS and an empirical runoff coefficient. *Hydrol. Res.* **51**, 1238–1260 (2020).
73. Herdendorf, C. E. Large lakes of the world. *J. Great Lakes Res.* **8**, 379–412 (1982).
74. Saltelli, A. et al. Variance based sensitivity analysis of model output. Design and estimator for the total sensitivity index. *Comput. Phys. Commun.* **181**, 259–270 (2010).
75. Fowler, H. J. et al. Anthropogenic intensification of short-duration rainfall extremes. *Nat. Rev. Earth Environ.* **2**, 107–122 (2021).
76. Eyring, V. et al. Overview of the Coupled Model Intercomparison Project Phase 6 (CMIP6) experimental design and organization. *Geosci. Model Dev.* **9**, 1937–1958 (2016).
77. Volkholz, J., Lange, S., & Geiger, T. ISIMIP3b population input data (v.1.1). ISIMIP <https://doi.org/10.48364/ISIMIP.889136.1> (2022).
78. Lesk, C. S. & Mankin, J. S. More concentrated precipitation decreases terrestrial water storage. Source data. Zenodo <https://doi.org/10.5281/zenodo.19116027> (2026).
79. Lesk, C. S. & Mankin, J. S. More concentrated precipitation decreases terrestrial water storage. Source code. Zenodo <https://doi.org/10.5281/zenodo.19191145> (2026).

Acknowledgements We thank Dartmouth Research Computing for computational support; and the participants of the Harvard Continental Climate Workshop held at Harvard University on 15–16 June 2023 and the Aspen Global Change Institute ‘Future of Terrestrial Water Availability’ workshop on 20–25 October 2024 for providing feedback. We acknowledge the World Climate Research Programme, which coordinated CMIP6; the climate modelling groups for producing and making available their model output; the Earth System Grid Federation for archiving the data; and the funding agencies for supporting CMIP6 and the Earth System Grid Federation. This research received funding from the Fonds de recherche du Québec—Nature et technologies award no. 31916 (C.S.L.), Dartmouth Neukom Institute for Computational Science (C.S.L. and J.S.M.), NOAA MAPP NA20OAR4310425 (J.S.M.), NSF CLD 2304953 (J.S.M.), DOE DESC0022302 (J.S.M.) and The Rockefeller Center (J.S.M.). The funders had no role in study design, data collection and analysis, decision to publish or preparation of the manuscript.

Author contributions C.S.L. and J.S.M. conceptualized the study and devised the methodology. C.S.L. conducted the analysis and visualized the study. C.S.L. and J.S.M. helped with funding acquisition. C.S.L. and J.S.M. wrote the paper.

Competing interests The authors declare no competing interests.

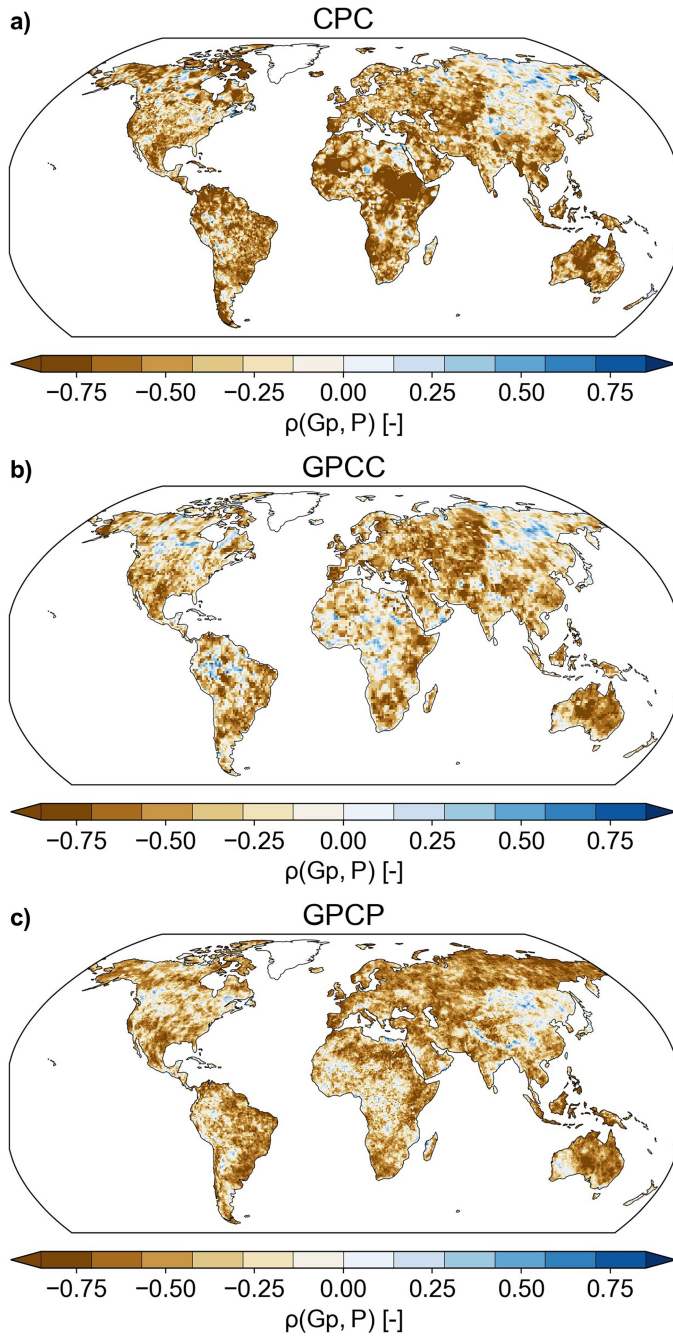
Additional information

Supplementary information The online version contains supplementary material available at <https://doi.org/10.1038/s41586-026-10487-7>.

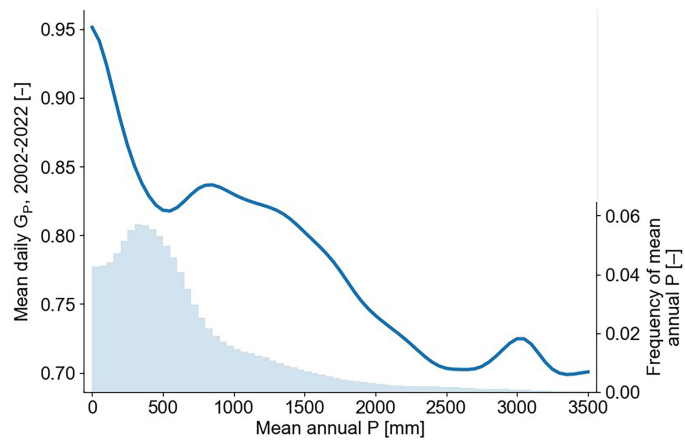
Correspondence and requests for materials should be addressed to Corey S. Lesk.

Peer review information Nature thanks Richard Allan, Marshall Burke, Sujay Kumar and the other, anonymous, reviewer(s) for their contribution to the peer review of this work. Peer reviewer reports are available.

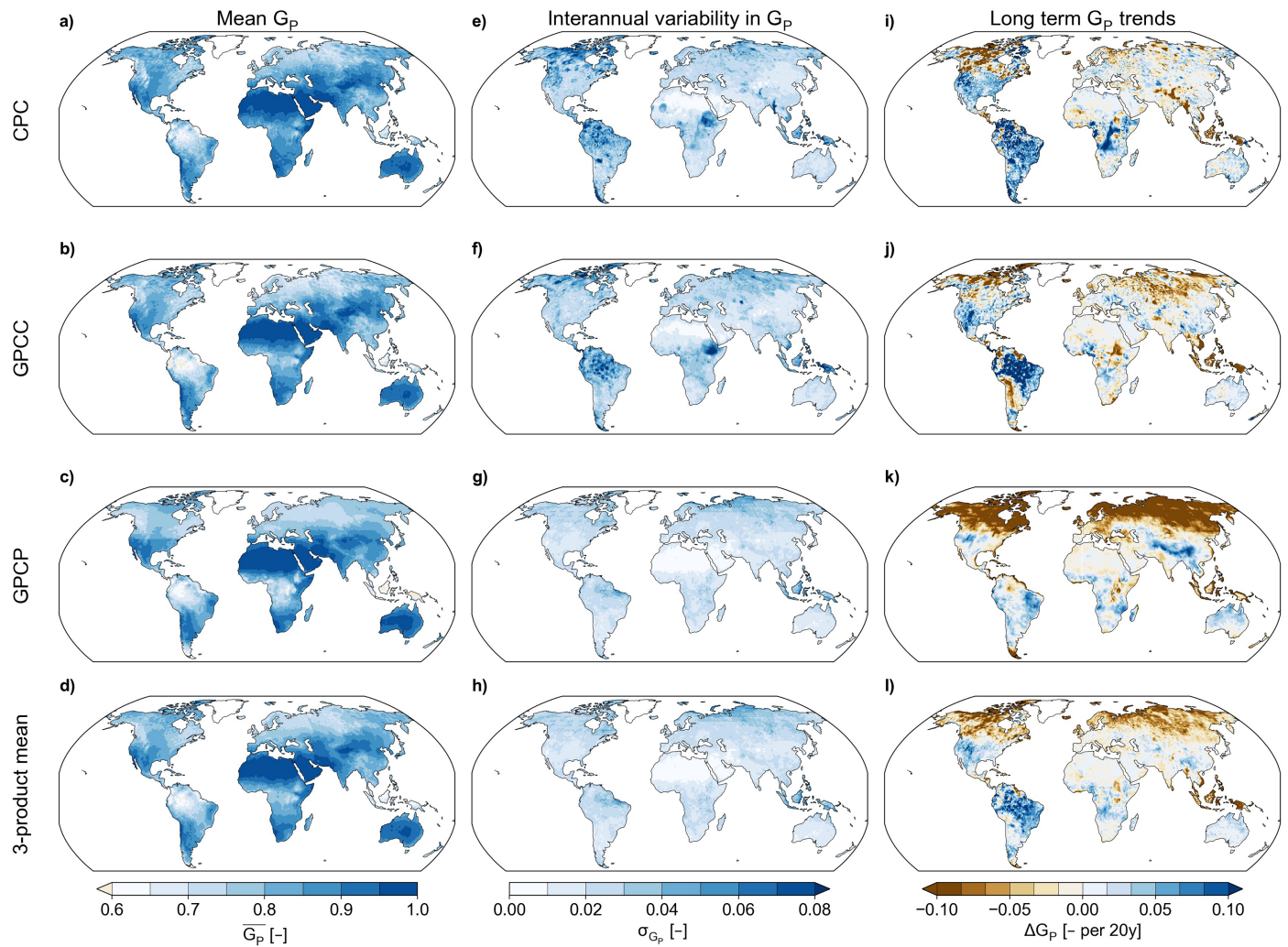
Reprints and permissions information is available at <http://www.nature.com/reprints>.



Extended Data Fig. 1 | Relationship between precipitation concentration and annual total precipitation. Local interannual Pearson correlation coefficients between the daily precipitation Gini index (G_p) and annual total precipitation for the a) CPC, b) GPCC, and c) GPCP daily precipitation datasets (refs. 21–23). Base map adapted from Natural Earth (<https://www.naturalearthdata.com>).

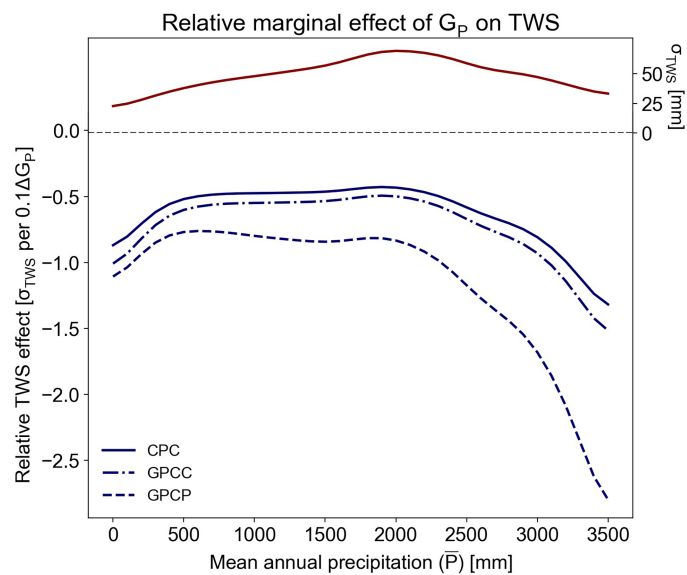


Extended Data Fig. 2 | Distribution of mean annual precipitation and daily precipitation concentration across global land area. Climatological G_p averaged over 100 mm bins of climatological annual precipitation across the global domain (blue curve, left vertical axis). Histogram of climatological annual precipitation in frequency terms (bars, right vertical axis). Data are from the CPC (ref. 22).

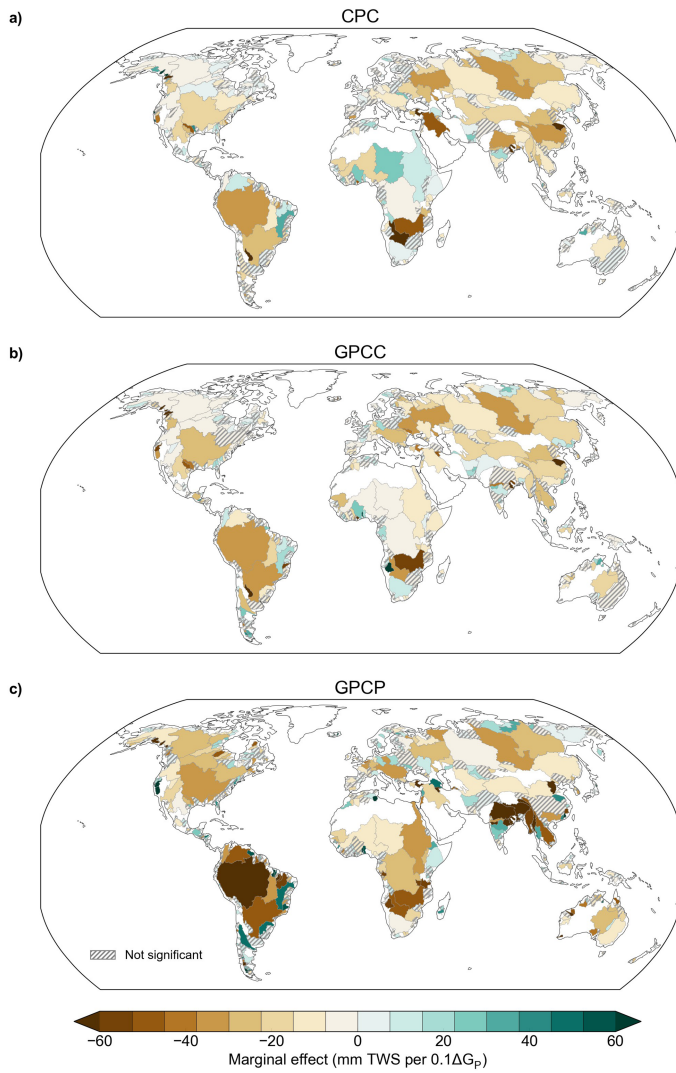


Extended Data Fig. 3 | Mean, variability, and trends in precipitation concentration across datasets. a-d) Full record climatological mean G_p for individual daily precipitation data products (CPC, GPCC, and GPCP, refs. 21–23, a-c) and for the three-product mean (d). e-g) Standard deviation of detrended G_p anomalies over the complete record length, as a metric of interannual

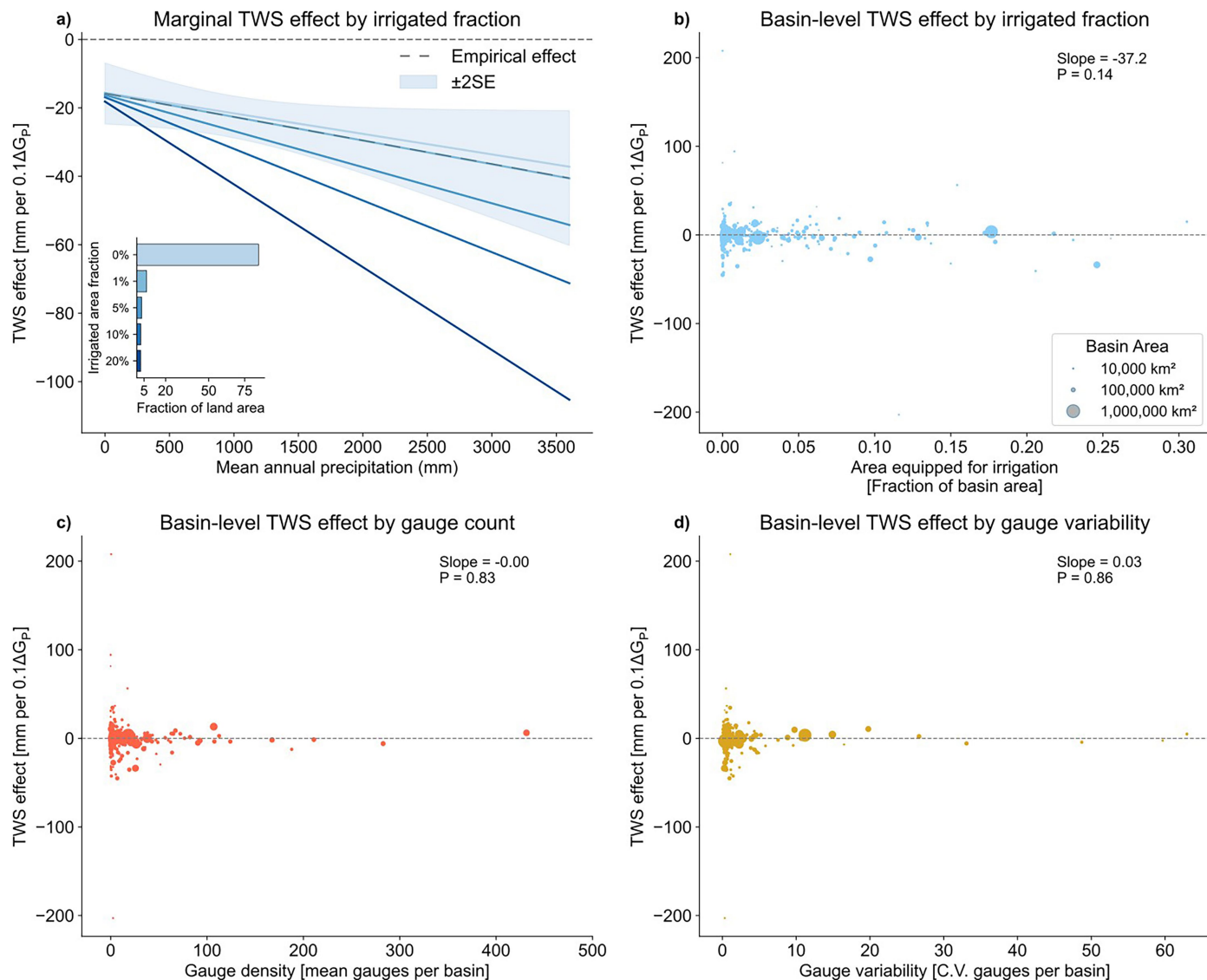
variability in precipitation concentration. i-l) Long-term linear trends in G_p , expressed as changes per 20 years (to harmonize across the varying record lengths of the three data products). Panels d and l are identical to Fig. 1f and g. Base map adapted from Natural Earth (<https://www.naturalearthdata.com>).



Extended Data Fig. 4 | Relative effect of precipitation concentration on terrestrial water storage. Interannual standard deviation of detrended GRACE TWS anomalies (ref. 25), averaged over 100 mm bins of climatological annual precipitation across its global domain (red curve, right vertical axis). Marginal effect of precipitation concentration on TWS, conditional on climatological precipitation (i.e., the effects in Fig. 2b), normalized by TWS standard deviation (blue curves, left vertical axis). This normalization estimates the magnitude of the TWS effect relative to local TWS variability (σ_{TWS}), as opposed to in absolute terms (mm, as in Fig. 2b).



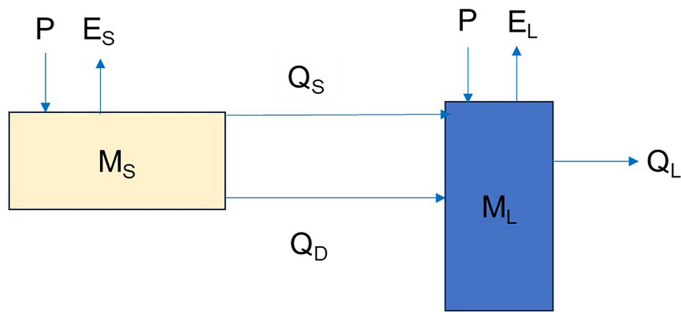
Extended Data Fig. 5 | Basin-level effects of concentration on terrestrial water storage across precipitation data products. Marginal G_p effects on TWS estimated at the scale of HydroSHEDS main river basins (ref. 51), as in Fig. 2c, but for individual precipitation data products. Estimated G_p coefficients of TWS are statistically significant ($p < 0.05$) except in hatched basins. Base map adapted from Natural Earth (<https://www.naturalearthdata.com>).



Extended Data Fig. 6 | Irrigation and gauge coverage dependence of precipitation concentration effects on terrestrial water storage. a) Marginal TWS effect of precipitation concentration, conditioned on grid cell-level area equipped for irrigation. Estimated TWS effects are shown for bins of area equipped for irrigation (lines). Inset histogram displays the percentage of global land area falling into each irrigated area bin. b-d) Basin-level TWS effect versus b) fractional basin area equipped for irrigation; c) spatial coverage of ground-based precipitation gauges, quantified as the mean number of GPCC

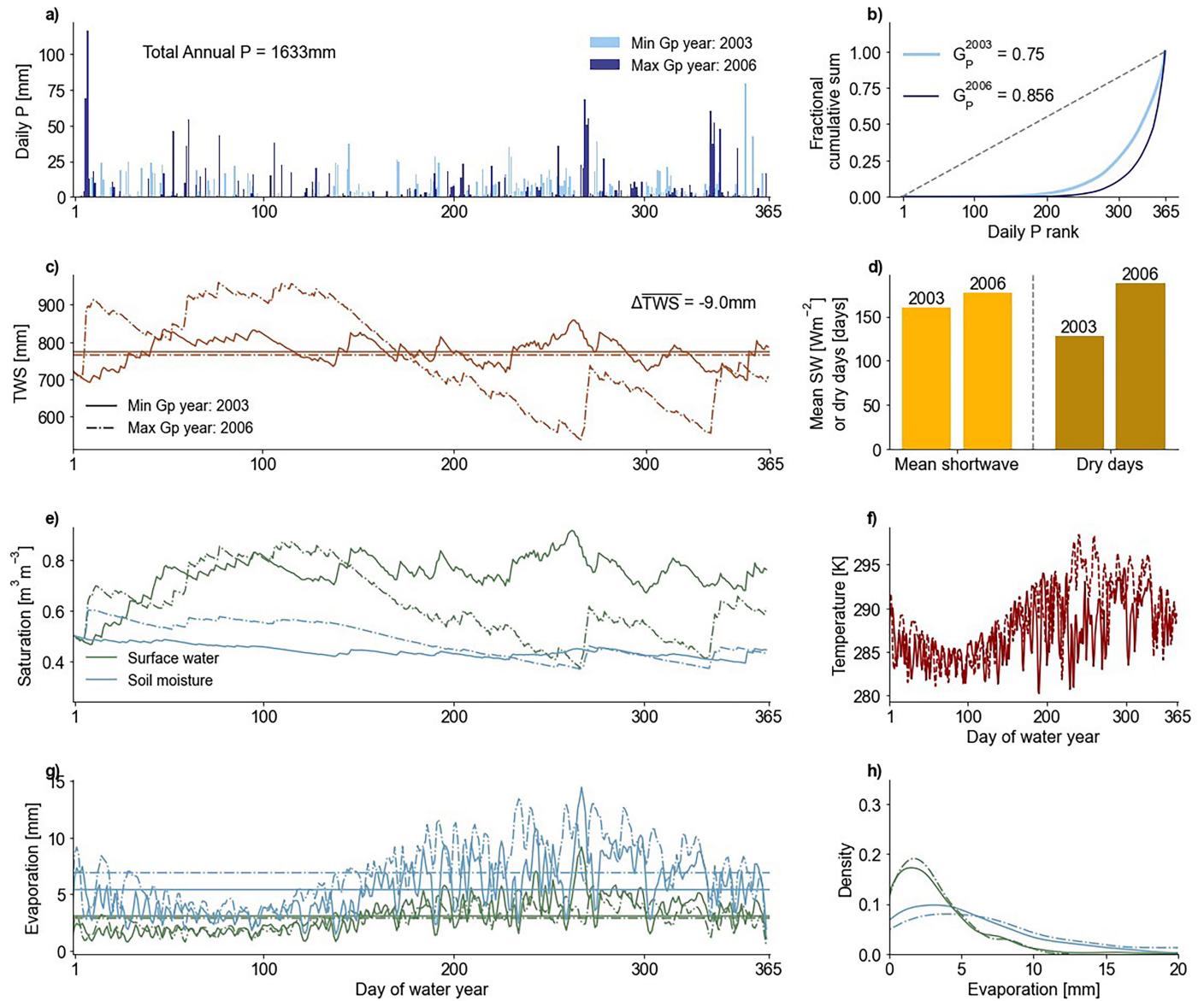
gauge per basin over 2002–2022 (ref. 23); and d) temporal variability of gauge number per basin, quantified as the coefficient of variation (time standard deviation over time mean gauges per basin). TWS effects are averaged across CPC, GPCC, and GPCP datasets (refs. 21–23). Irrigation data in a-b) are derived from UN Food and Agriculture AQUASTAT Global Information System on Water and Agriculture. Annotations in b-d) are univariate linear regression coefficients; basin scale TWS effects are drawn from the data in Fig. 2c; and the size of the points is proportional to basin area.

Article



Extended Data Fig. 7 | Schematic of hydrologic stocks and fluxes in idealized land-surface model. M_S and M_L denote the soil and surface water stocks, while arrows denote fluxes. P is precipitation; E_S , soil evaporation; E_L evaporation from the surface water stock; Q_S , surface ponding rate of precipitation (infiltration and saturation excess); Q_D , soil drainage; and Q_L , runoff. In this formulation, Q_S is considered a flux internal to the modeled location, while flows out from the surface water stock are classified as runoff (i.e., export).

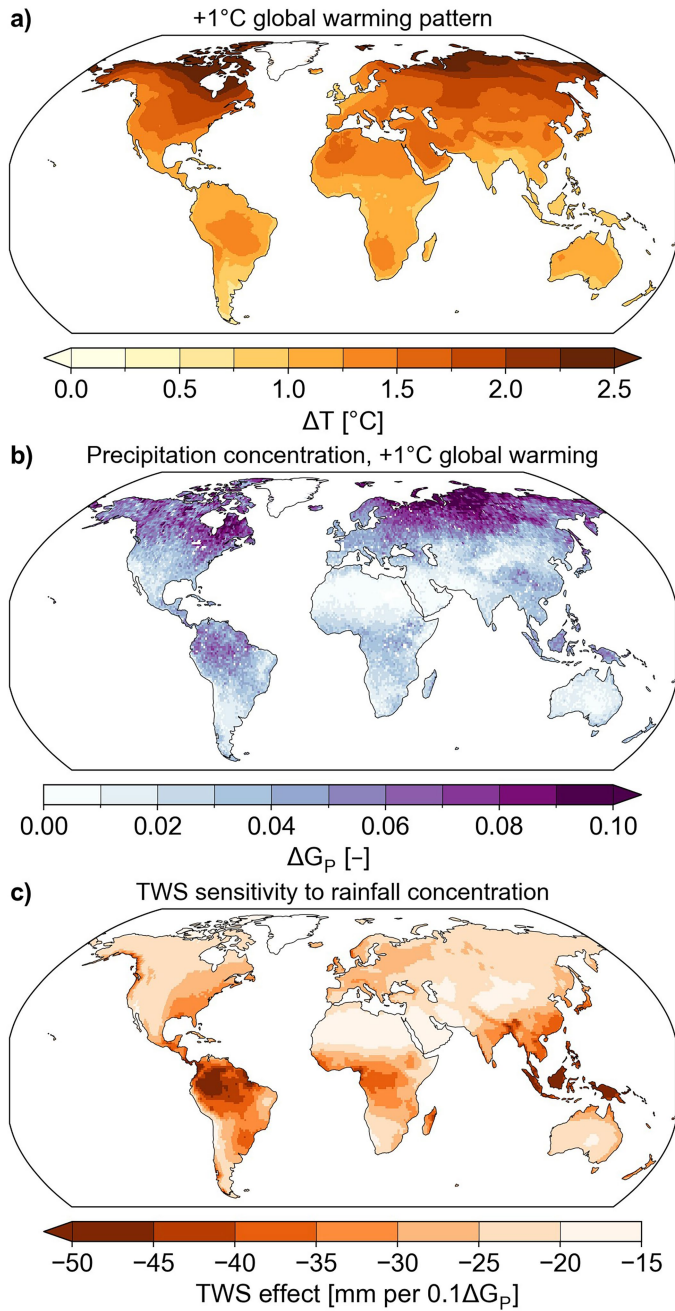
SEMB-H idealized land model, forcings & output: Eastern US (280.5°E, 37.5°N)



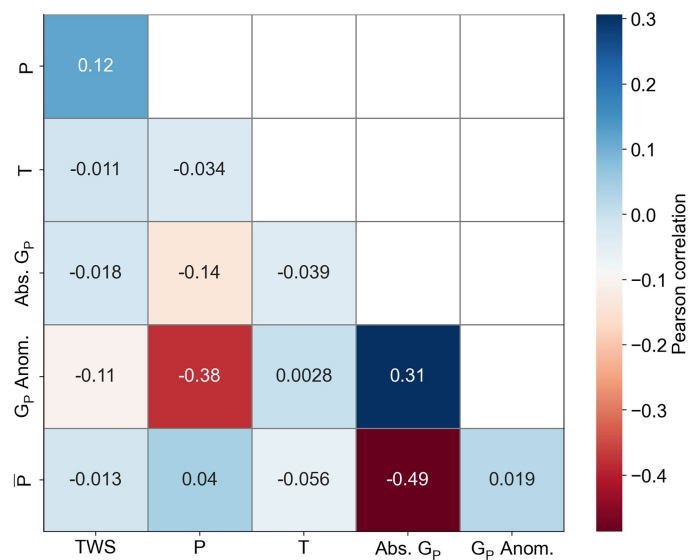
Extended Data Fig. 8 | Sample simulation from the idealized land-surface model. Illustrative output from the Surface Energy and Moisture Balance Model with Hydrology (SEMB-H) run with daily precipitation and shortwave forcings from CPC (ref. 22) and GEWEX-SRB (ref. 52) for the point 280.5°E, 37.5°N (near Roanoke, Virginia, US). Model output contrasts between the highest and lowest G_p years (2006 and 2003). a) Daily precipitation forcing time series for the two years, with daily values scaled such that the two time-series sum to equal annual total precipitation (1633 mm). b) Daily precipitation Lorenz curves for the two years, with corresponding G_p values annotated. c) Simulated TWS evolution, with horizontal lines denoting annual mean TWS. d) Annual

mean shortwave radiation and total dry days for the high and low G_p years. e) Daily evolution of the simulated surface water (blue) and soil moisture (green) stocks, in terms of fractional saturation. f) Daily evolution of simulated surface air temperature. g) Evolution of simulated evaporation from surface water and soil moisture stocks. h) Frequency distribution of daily evaporation from surface water and soil moisture stocks. We track the difference in annual mean TWS between the highest and lowest G_p years (in this example, -9mm) as equivalent measure to GRACE TWS anomalies used in our panel regression. Solid and dashed lines denote the minimum and maximum G_p years in c and e-h.

Article



Extended Data Fig. 9 | Drivers of precipitation concentration and terrestrial water storage impacts under an additional 1°C of global warming. a) Mean surface air warming pattern at 1°C of global warming, derived from the 26 general circulation and Earth system simulations from the Coupled Model Intercomparison Project, Phase 6 (CMIP6, ref. 76), run under the SSP5-8.5 scenario. b) G_p changes for precipitation concentration under warming from a), projected using a thermodynamic rainfall intensification model. c) TWS sensitivity to precipitation concentration, conditioned on climatological precipitation, as estimated from the panel regression model (averaged across the three precipitation datasets). Base map adapted from Natural Earth (<https://www.naturalearthdata.com>).



Extended Data Fig. 10 | Correlation among hydroclimate drivers of terrestrial water storage variability. Pairwise Pearson correlation among the hydroclimate predictors and TWS. All variables except absolute G_p and climatological mean precipitation (P) are in terms of detrended anomalies, and the correlation is calculated for pooled grid points over space and time.